Appl. Phys. A (2005)
DOI: 10.1007/s00339-005-3256-7

Applied Physics A
Materials Science & Processing

Invited paper

A.A. PURETZKY[1,2,✉]
D.B. GEOHEGAN[1]
S. JESSE[1]
I.N. IVANOV[1,2]
G. ERES[1]

In situ measurements and modeling of carbon nanotube array growth kinetics during chemical vapor deposition

[1] Condensed Matter Sciences Division, Oak Ridge National Laboratory, Oak Ridge, TN 37831-6056, USA
[2] Department of Materials Science and Engineering, University of Tennessee, Knoxville, TN 37996, USA

Received: 3 March 2005/Accepted: 14 March 2005
Published online: 20 April 2005 •

ABSTRACT Direct measurements of carbon nanotube growth kinetics are described based upon time-resolved reflectivity (TRR) of a HeNe laser beam from vertically aligned nanotube arrays (VANTAs) as they grow during chemical vapor deposition (CVD). Growth rates and terminal lengths were measured in situ for VANTAs growing during CVD between 535 °C and 900 °C on Si substrates with evaporated Al/Fe/Mo multilayered catalysts and acetylene feedstock at different feedstock partial pressures. Methods of analysis of the TRR signals are presented to interpret catalyst particle formation and oxidation, as well as the porosity of the VANTAs. A rate-equation model is developed to describe the measured kinetics in terms of activation energies and rate constants for surface carbon formation and diffusion on the catalyst nanoparticle, nanotube growth, and catalyst over-coating. Taken together with the TRR data, this model enables basic understanding and optimization of growth conditions for any catalyst/feedstock combination. The model lends insight into the main processes responsible for the growth of VANTAs, the measured number of walls in the nanotubes at different temperatures, conditions for growth of single-wall carbon nanotube arrays, and likely catalyst poisoning mechanisms responsible for the sharp decline in growth rates observed at high temperatures.

PACS 61.46.+w; 81.07.De; 81.16.Hc

1 Introduction

Chemical vapor deposition (CVD) is an attractive approach for growing single- and multi-wall carbon nanotubes (SWNTs/MWNTs). As a result, numerous empirical attempts have been taken to optimize the CVD growth by choosing an appropriate catalyst, supporting substrate, CVD gases, flow rates, synthesis temperature, etc. In addition to the optimal growth conditions, precise control over the nanotube length, number of walls, and diameter is important for the many applications of nanotubes in electronic devices and sensors [1], as well as for their use in composites [2]. Although these empirical studies produced some useful growth recipes and inspired many theoretical discussions about the growth mechanisms, they were unable to provide a clear path to the understanding of the growth mechanisms. The nanotube growth mechanisms and kinetics are the subject of much speculation, mainly because of the lack of in situ diagnostic techniques that can be employed in the typical CVD environment. At present, the growth rates and ultimately the lengths of nanotubes are limited by unknown factors, which has great bearing on applications.

The necessity of in situ monitoring of carbon nanotube (filament) growth has been understood for quite some time. Baker observed in situ the manner by which various metal and alloy particles catalyze the growth of carbon filaments using controlled atmosphere electron microscopy [3]. In this approach samples for in situ growth monitoring were prepared in the form of supported metal catalyst films, about a monolayer thick. The films nucleated into nanometer-size particles (5–20 nm in diameter) during sample heating.

Recently, Helveg et al. used high-resolution in situ transmission electron microscopy (TEM) to observe the growth of carbon nanofibers with atomic resolution [4]. In this work CH_4 was decomposed over $MgAl_2O_4$-supported Ni nanocrystals at 500 °C. Many new interesting features of the nanofiber growth were revealed by this study, such as a reaction-induced reshaping of the Ni nanocrystals during growth, formation and propagation of the step edges at the surface of the nickel nanoparticles, etc.

Bonard et al. attempted to develop in situ diagnostics of MWNT growth by performing field-emission microscopy directly in a modified CVD reactor. They found that MWNTs grow after an activation time of a few seconds with growth rates of 1–10 μm/s [5]. However, the interpretation of these results is not straightforward and the technique is limited to very low pressures.

Recently, we developed a simple and powerful approach for in situ monitoring of growth of vertically aligned nanotube arrays (VANTAs), based on time-resolved reflectivity (TRR) [6]. Attenuation of a reflected HeNe laser beam and Fabry–Perot fringes were used to measure the length of VANTAs throughout the first 10 microns of growth. A similar technique was applied recently to monitor carbon nanotube growth using plasma-enhanced CVD [7].

VANTAs have been grown in patterned arrays by CVD using lithographically patterned catalyst films, solutions, or materials to which the floating catalyst will stick [1, 2, 8–13].

✉ Fax: +1-865-576-3676, E-mail: 1ap@ornl.gov

The average growth rates reported for the VANTAs range from 0.4 to 50 μm/min [8, 9] with lengths typically terminating around 50–200 μm [1, 2, 10]; however, lengths of 1.5–3 mm have been achieved [8, 10, 13].

In our in situ TRR monitoring of the VANTA growth, electron-beam-evaporated multi-layered metal catalysts (Fe/Mo) were deposited on a Si substrate with an Al underlayer [6]. This catalyst system was developed by Delzeit et al. and was used to grow both SWNTs [14] and vertically aligned multi-wall nanotubes (VA-MWNTs) [11].

In this paper we describe the application of TRR for in situ monitoring of the catalyst film pretreatment and growth of VANTAs. To demonstrate the power of the TRR technique we provide a detailed experimental study of the growth rates of VANTAs in the temperature range from 535 to 900 °C, and variable concentrations of the C_2H_2 feedstock gas. We obtain the time evolution of the heights of VANTAs at different growth temperatures, and demonstrate that the growth stops rapidly at relatively low (535–600 °C) as well as at high (800–900 °C) temperatures, exhibiting a relatively narrow temperature window for the optimal growth of long VANTAs (up to a few millimeters) around 700 °C at a growth rate of about 0.2–0.5 μm/s. We also observe that the growth termination length can be increased by decreasing the partial pressure of the C_2H_2 feedstock gas. We found that the type of the nanotubes grown on the multi-layered metal catalyst changes in the temperature range from 535 to 900 °C. The thicker, more defective VANTAs with 6–10 walls are grown at 575 °C, while predominantly double-walled nanotubes (DWNTs) were found at 725 °C. Above 700 °C, the Raman spectra show strong features of SWNTs/DWNTs.

Finally, we describe a kinetic model to explain the time evolution of the heights of VANTAs, the temperature dependence of the growth rates, the terminal lengths, and the number of walls based on the processes that are responsible for the observed effects in VANTA growth.

The paper is arranged as follows. Section 2 describes the experimental setup (Sect. 2.1) and the TRR technique for in situ monitoring of the multi-layered metal catalyst pretreatment (Sect. 2.2) and carbon nanotube growth (Sect. 2.3). Section 3 describes the experimental procedure used to calibrate successive Fabry–Perot fringes using an arrested growth approach. Section 4 provides a theoretical interpretation of the observed interference fringes in the frame of an effective-medium approximation for VANTAs. In this section we calculate the reflectance and transmittance of VANTAs and estimate their porosity. Section 5 is devoted to the experimental study of the growth rates of VANTAs at different temperatures and concentrations of the C_2H_2 feedstock gas. Section 6 summarizes the results of the Raman spectroscopy study of carbon nanotubes at different temperatures. Section 7 focuses on the discussion of the main processes involved in VANTA growth based on the kinetic model. The main conclusions of this work are provided in Sect. 8.

2 Experiment and method

2.1 *Experimental setup*

The catalyst system used for VANTA growth consisted of multi-layered metal films (10 nm of Al, 1 nm of Fe, and 0.2 nm of Mo) prepared by electron-beam evaporation onto Si(100) substrates. Sputtered films of this catalyst system were used by Delzeit et al. with ethylene to grow VA-MWNTs and SWNTs on various substrates [11, 14]. Recently, we characterized the growth of MWNTs and SWNTs on Si substrates with this catalyst system using acetylene [15]. The substrate with the metal films was mounted vertically, perpendicular to the gas-flow direction, using a fused-silica mount in the center of a CVD tube. A schematic diagram of a CVD reactor is shown in Fig. 1. The CVD reactor consists of a quartz tube (3-in diameter, 4-ft length) placed inside a high-temperature furnace (Lindberg/Blue, model HTF55342C, maximum temperature 1200 °C, 35-in length, 8-in uniform-temperature zone). The CVD reactor was equipped with four mass-flow controllers (Hitachi, model SFC-460, 10 sccm H_2 maximum flow rate, and model 480, 100 sccm, 500 sccm, and 2000 sccm Ar maximum flow rates) and an automatic pressure-control system. A thermocouple was located in the center of the furnace near the outer quartz tube surface. The temperature of the Si substrate was also measured using a single-color pyrometer (IRCON, model W-10C10, $\lambda = 0.9$ μm, temperature range 400–1000 °C) through a quartz view port located at the exit end of the quartz tube. The entrance port of the quartz tube was equipped with a glass window (4-in diameter) to permit the entry and exit of a stabilized HeNe laser beam ($\lambda = 632.8$ nm, 4 mW, Laboratory for Science, model 200) as shown in Fig. 1b. The intensity of the beam reflected from the substrate and the growing VANTA was recorded with a silicon photodiode and a computer-interfaced digital multimeter (Keithley 196) with a time resolution of 140 ms. The diameter of the HeNe laser beam spot on the Si substrate was 2 mm.

The nanotubes were characterized using scanning electron microscopy (SEM) (Hitachi S-4700 field-emission SEM), transmission electron microscopy (TEM) (Hitachi HF-2000), and Raman spectroscopy. The Raman spectra were measured using a micro-Raman spectrometer (Renishaw Inc., model RM1000) in the backscattering configuration. A HeNe laser

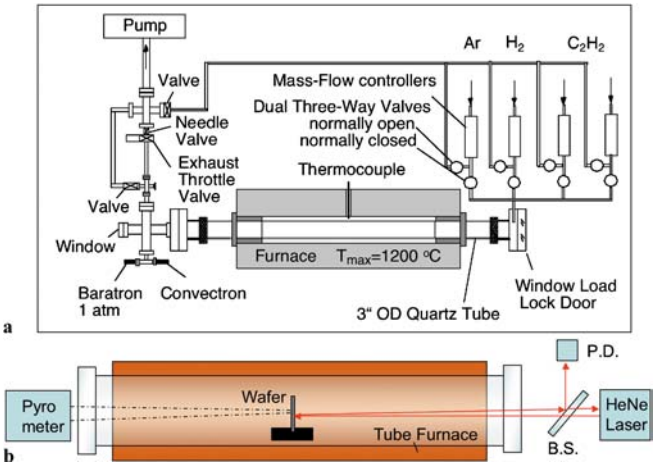

FIGURE 1 (**a**) A schematic of the CVD setup with (**b**) in situ time-resolved reflectivity monitoring of VANTA growth. The CVD reactor consists of a quartz tube placed inside a high-temperature furnace and is equipped with mass-flow controllers and an automatic pressure-control system. The entrance port of the quartz tube is equipped with a glass window to permit the entry and exit of a stabilized HeNe laser beam for in situ TRR diagnostics of VANTA growth

($\lambda = 632.8$ nm, maximum 3 mW laser power on a sample, ~ 2 μm laser spot, ×50 objective, NA 0.75) was used for excitation. In most cases, the spectra were measured using a 10-s accumulation time.

The surface morphology of the Si–metal layer films before and after a high-temperature annealing step was characterized using an atomic force microscope (AFM) (Digital Instruments, MultiMode NS-IIIA).

2.2 *In situ reflectivity monitoring of catalyst films during pretreatment*

The goal of the pretreatment procedure is to convert a catalyst film to nanoparticles and to stabilize the temperature at the chosen level for carbon nanotube growth. A Si substrate with the catalyst film was heated in flowing Ar (Air Liquide, 99.9997% pure, 2000 sccm flow rate) and H_2 (Air Liquide, 99.9995% pure, 400 sccm flow rate at atmospheric pressure) to the growth temperature. Figure 2a and b show the time evolution of the oven temperature and the reflected light intensity during pretreatment at the targeted growth temperature of 575 °C. It takes about 10 min for the temperature to reach the set value. After the furnace reaches the set temperature, an additional 10 min are allowed for the temperature to equilibrate at the set temperature.

During the ramp-up of the furnace temperature, the reflected intensity slowly decreases starting from $T \geq 230$ °C followed by a relatively sharp drop at $T \sim 400$–410 °C. After the sharp transition, the reflected intensity slowly reaches a plateau, corresponding to $\sim 50\%$ of the initial intensity (Fig. 2a and b). This intensity is approximately equal to the reflected light intensity from a bare Si substrate measured at the equilibrium temperature (575 °C).

Note that Fig. 2b shows the temperature measured by the furnace thermocouple (Fig. 1a). The actual temperature of the Si–metal film substrate may be different from that measured by the thermocouple. Direct pyrometer-based measurement of the Si-substrate temperature during ramp-up (usually ~ 100 °C/min) of the furnace temperature is inaccurate because of strong interference by radiation emitted from the furnace coils, reflected by the Si substrate, and detected by the pyrometer in addition to the Si-substrate black-body radiation. When the furnace temperature stabilizes, the current through the furnace coils drops significantly. At this point, the temperature of the Si substrate can be measured using the pyrometer. We found that at these conditions the pyrometer and the thermocouple readings were in good agreement. To estimate the temperature difference between the Si substrate and the furnace thermocouple during the ramp-up, the Si/Al/Fe/Mo substrate was heated using a very slow temperature ramp, 5 °C/min, in order to provide enough time for the temperature to reach equilibrium. Figure 3a shows the plot of the reflected intensity vs. temperature measured by the furnace thermocouple for two different ramping rates, 90 °C/min and 5 °C/min. At 5 °C/min the sharp reflectivity drop occurs at a slightly higher temperature (~ 46 °C) than in the rapid heating case. This means that, during our regular rapid heating pretreatment (~ 100 °C/min), the actual temperature of the Si substrate could be ~ 50 °C higher compared to that recorded by the furnace thermocouple.

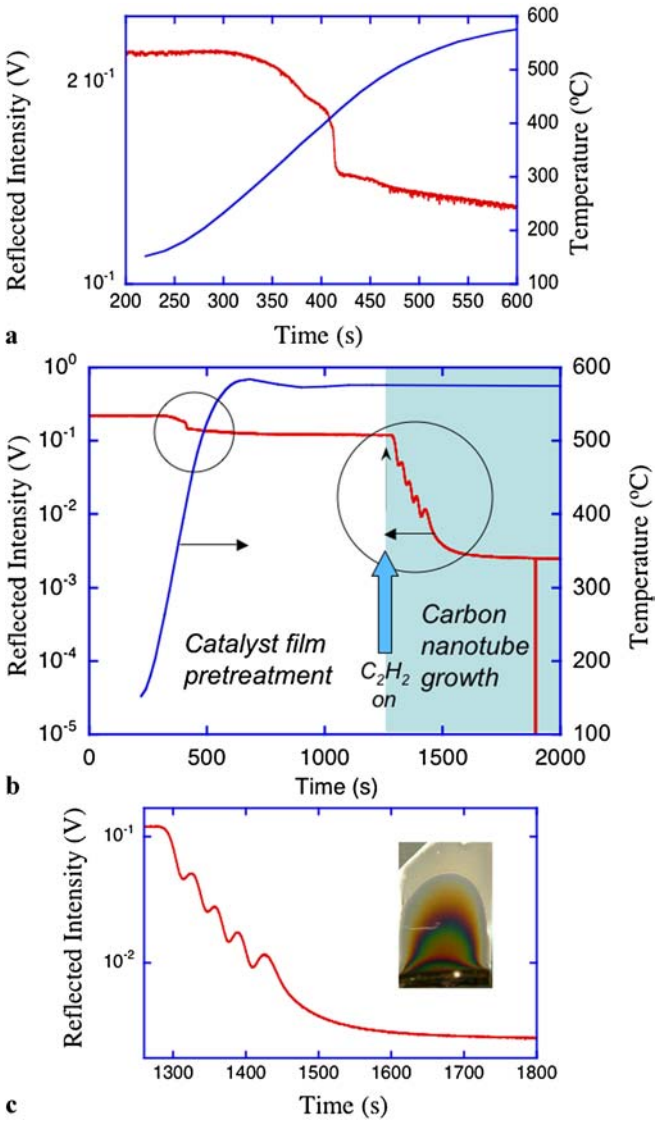

FIGURE 2 (**a**), (**b**) – *left-hand frame* Intensity of the specularly reflected HeNe laser beam and the oven temperature during pretreatment and ramp-up to the targeted growth temperature of 575 °C. (**b**) – *right-hand frame*, (**c**) Time evolution of the reflected laser intensity during VANTA growth. C_2H_2 gas was added to the flowing Ar (2000 sccm) and H_2 (400 sccm) gas mixture at 6 sccm. After ~ 26 s the reflected beam intensity decreases exponentially, displaying reproducible oscillations during the 1286–1500 s time interval. At $t \geq 1500$ s, the reflected intensity does not change significantly, indicating termination of VANTA growth. The *vertical line* around 1900 s (**b**) shows the minimum photodiode signal ($\sim 10^{-5}$ V) that could be detected, indicating the dynamic range of about four orders of magnitude available for the reflected light intensity measurements. The *inset* in (**c**) shows an image of a VANTA film on a Si substrate, displaying a thickness gradient along the vertical direction and exhibiting colored interference fringes

Figure 3b shows the reflected intensity vs. temperature plot for two different equilibrium temperatures, 575 °C and 700 °C. The reflected intensity decreases slowly in the temperature range from 150 °C to ~ 400 °C followed by a relatively sharp drop around 400 °C, a small plateau, and a further decrease to the final reflectivity level of the Si substrate ~ 0.5. Since the reflectivity of the Si substrate does not change much in the studied temperature range, the observed changes in reflectivity are related to the deposited metal films, most likely to the thickest 10-nm Al film.

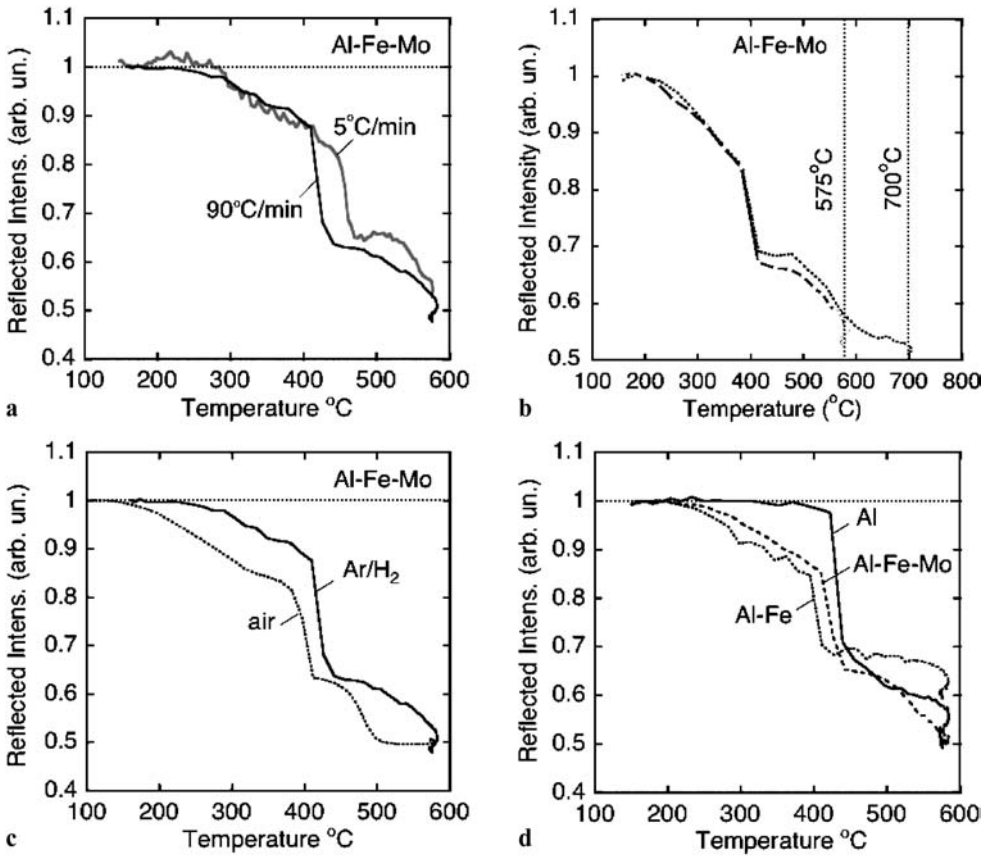

FIGURE 3 Intensity of the specularly reflected HeNe laser beam vs. measured furnace temperature; (**a**) using two different ramp-up rates, 90 °C/min and 5 °C/min, (**b**) during the pretreatment cycle at two targeted temperatures, 575 °C (*solid line*, *open circles*) and 700 °C (*dotted line*). The *dotted vertical lines* show two equilibration temperatures used for further VANTA growth, (**c**) in air compared to Ar/H_2, (**d**) using different metal films, Al (10 nm), Al–Fe (10 nm–1 nm), and Al–Fe–Mo (10 nm–1 nm–0.2 nm)

At least three different mechanisms can be responsible for the observed changes in the reflectivity during heating: (1) the temperature dependence of metal dielectric constants, (2) the melting of nanometer thin metal films and their alloys, and (3) the roughening of the metal films due to oxidation.

The theory of reflectivity of metals at high temperatures was considered by Ujihara [16] in the frame of the Drude model for the metal dielectric constants. The reflectivity of Al in the temperature range of 25–600 °C was calculated numerically, starting with $N_{Al} = 1.55 + 7.00i$ (at $\lambda = 0.69$ nm, $T =$ 102 °C) [16]. These calculations show that the Al reflectivity drops from ∼ 0.8 (at 27 °C) to ∼ 0.6 (at 600 °C).

To understand whether the changing of the Al reflectivity was responsible for the observed reflectivity changes vs. temperature, a series of Si/Al/Fe/Mo substrates were first heated to different temperatures, from 300 °C to 450 °C, and then cooled to ∼ 150 °C.

Figure 4 shows the results of this temperature-cycling experiment. A hysteresis-type behavior was observed in all cases, indicating that irreversible changes in reflectivity occur even at the lowest temperature of ∼ 300 °C.

If the temperature variation of the Al dielectric constant is responsible for the initial drop of the reflectivity, temperature cycling should be reversible. For surface roughening, due to oxidation, the change of the reflectivity should be irreversible. The irreversible behavior of the experimental reflectivity curves suggests that the oxidation-induced surface roughening is the main mechanism leading to the observed drop in the reflectivity in this temperature range. This conclusion is confirmed by the heating of the Si/Al/Fe/Mo substrate in air instead of Ar/H_2. Figure 3c shows that annealing in air indeed leads to a steeper initial reflectivity drop compared to that in Ar/H_2. Figure 3d shows that the reflectivity of pure Al films behaves quite differently during annealing compared to that of Al/Fe and Al/Fe/Mo thin films. Only a small initial drop in the reflectivity is observed for a pure Al film in the temperature range from 150 °C to 400 °C compared to Al/Fe and Al/Fe/Mo films. This behavior can be explained by the formation of a thin protective layer of Al_2O_3 [17].

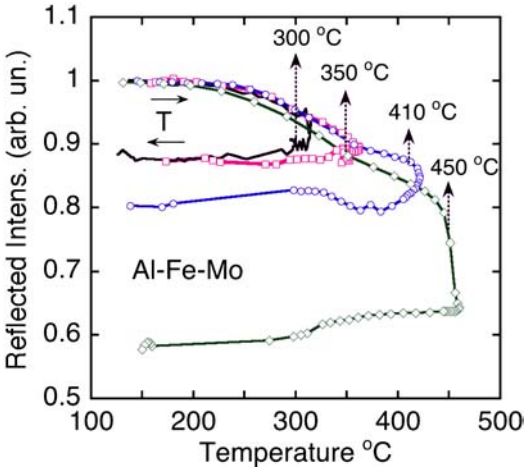

FIGURE 4 Reflected intensity vs. temperature during heating–cooling cycles of Al (10 nm)/Mo (0.2 nm)/Fe (1 nm) catalyst films to different final temperatures

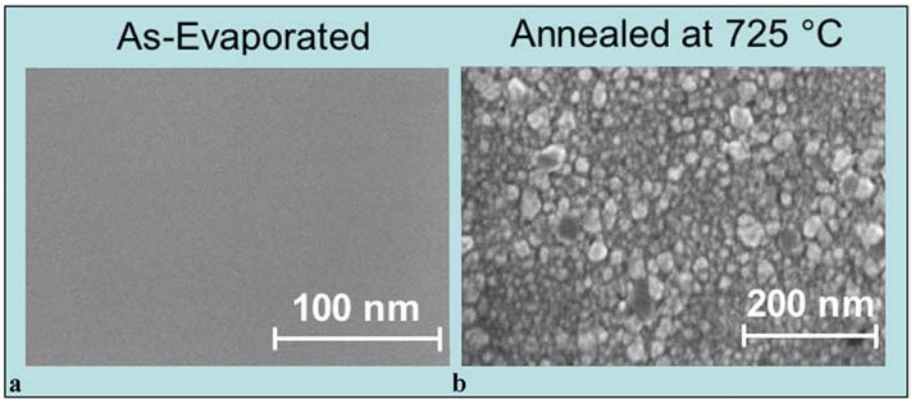

FIGURE 5 SEM images of Al (10 nm)/Mo (0.2 nm)/Fe (1 nm) catalyst films (**a**) as deposited by the electron beam evaporation technique and (**b**) after annealing at 725 °C

The sharp drop in reflectivity around 400 °C is related to surface roughening but involves an additional mechanism – melting of the residual aluminum (Fig. 3a–d) – which is discussed below.

The surface morphology of the Si substrate with the metal films was analyzed before and after the annealing pretreatment using an AFM (Digital Instruments, MultiMode NS-IIIA) and a SEM. The SEM image of a Si substrate with the catalyst films before annealing (Fig. 5a) does not show any obvious surface roughness. After annealing in Ar/H_2 the SEM image (Fig. 5b) shows a completely different surface morphology with well-resolved surface roughness. Figure 6a shows the AFM image of an as-deposited Si–catalyst substrate, exhibiting root mean square (rms) surface roughness, i.e. rms of height deviations taken from the mean data plane, of about 0.8 nm. Annealing to 300 °C (see Fig. 4) increases the rms surface roughness to 1.3 nm (Fig. 6b). Further increase in the annealing temperature to 410 °C results in a dramatic increase in the rms roughness to 4.8 nm (Fig. 6c). This temperature is close to the onset of the sharp transition in the reflectivity (Figs. 3 and 4). Annealing above the temperature of the sharp transition in the reflectivity leads to a decrease in the rms surface roughness. For example, at 450 °C the rms surface roughness is only 3.4 nm (Fig. 6d). Figure 7 summarizes these results and shows the dependence of the rms surface roughness on the annealing temperature. The rms surface roughness increases in the temperature range from 25 °C to 410 °C and then falls when the temperature exceeds 410 °C, which corresponds to the temperature of the sharp transition in the reflectivity.

The gradual increase of the surface roughness in the temperature range from 25 °C to 410 °C is related to formation of Al_2O_3 nanocrystals due to oxidation of the Al/Fe/Mo film. The oxidation decreases the thickness of the residual Al underlayer and also releases a considerable amount of heat [18] that can drive the surface temperature up to the melting point of Al, 600.4 °C, or to the eutectic temperature of Al–Si, 577 °C [19]. The Al film used in our case is too thick ($\sim$ 10 nm) to consider the effects of a size-dependent decrease of the melting point [20, 21], although it is plausible that initial oxidation-induced surface roughening results in nanometer-size Al particles that can melt at lower temperatures. As a result, the residual Al film melts, and the morphology of the catalyst film surface changes at $T > 410$ °C (Fig. 7). At higher temperatures the Al film oxidizes completely, forming

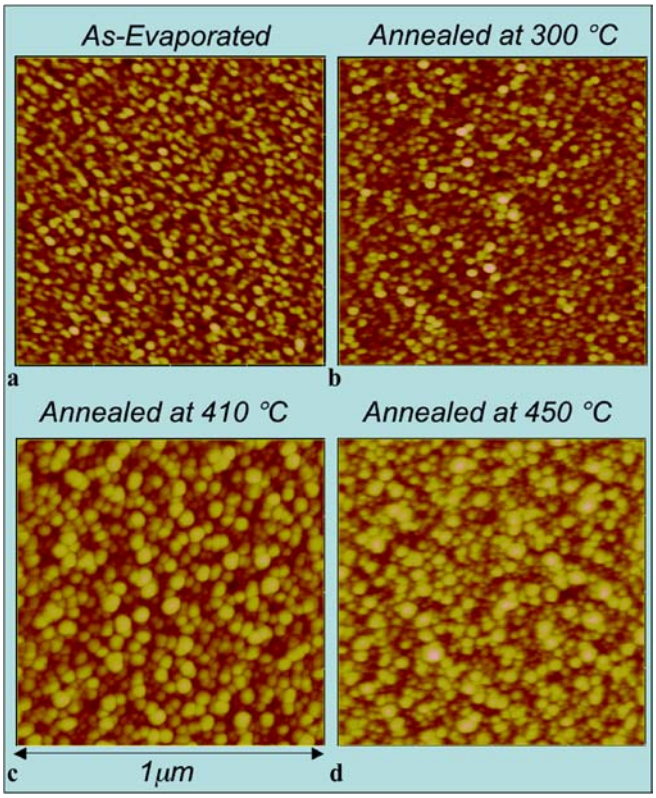

FIGURE 6 AFM images of Al (10 nm)/Mo (0.2 nm)/Fe (1 nm) catalyst films; (**a**) as-evaporated, (**b**) annealed at 300 °C, (**c**) annealed at 410 °C, and (**d**) annealed at 450 °C

a nanostructured Al_2O_3 matrix embedded with nanoparticles of Fe/Mo catalyst.

Recently, a detailed study of Al buffer layer oxidation effects on catalytic CVD growth of carbon nanotubes using in situ X-ray spectroscopy has been reported [22]. Oxidation of Al was shown to be necessary to prevent Fe from reactioning with the Si substrate and preventing nanotube growth. This observation supports our conclusion about extensive oxidation of the Al buffer layer during the annealing pretreatment procedure.

2.3 *Carbon nanotube growth*

After about 20 min of pretreatment, the temperature equilibrates and the reflected intensity remains constant.

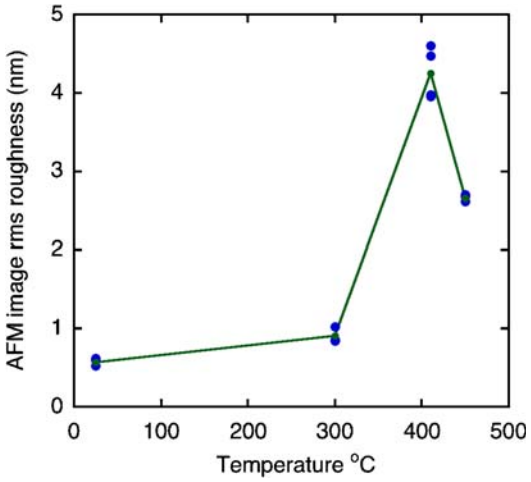

FIGURE 7 rms roughness of the Al/Mo/Fe films annealed at different temperatures

At this point (see Fig. 2b and c) a pre-established 6 sccm flow of C_2H_2 (Air Liquide, Alphagaz-1, 99.6% pure) was switched into the flowing Ar/H_2 gas mixture. As shown in Fig. 2c, 26 s later the reflected beam intensity began to decrease exponentially due to absorption and scattering by the growing nanotubes. In addition, the time-resolved reflected intensity displayed reproducible oscillations. Both the oscillations and the extinction of the beam can be used to monitor the length of the VANTAs.

The oscillations result from interference between light reflected from the top of the VANTA and light that is reflected from the Si substrate which passes twice through the nanotube forest. These Fabry–Perot fringes serve as fiducial markers that permit determination of lengths and growth rates during deposition. The inset in Fig. 2c shows colored films of VANTAs due to thickness interference. The observed patterns depend on the temperature gradient across the substrate during VANTA growth, which is determined by the way the substrate was mounted in the CVD reactor. The image in Fig. 2c corresponds to the case when the substrate was mounted vertically at its bottom edge, inserted in a slot of a pyrolytic graphite disk (1-in diameter) and placed in the center of the CVD reactor. In this case the temperature gradient is directed vertically along the substrate, since the top part of the substrate will have a slightly lower temperature, due to cooling by the gas flow, than the walls of the quartz tube and the substrate support. The temperature gradient results in thickness variations of the VANTA, which produce the colored interference patterns.

3 Length calibration of VANTAs using growth-stop experiments

The incremental length, d_0, for successive Fabry–Perot fringes corresponds to $\lambda/2n_{\text{eff}}$. Description of the length requires the effective index of refraction, n_{eff}, of the porous VANTAs, even in the case of the simplest assumption that VANTAs could be described by a single effective medium. A detailed description of this problem will be given in Sect. 4. In this section we provide direct experimental measurements of the incremental length, d_0, using an arrested growth approach.

Growth of the VANTAs was halted after different numbers of fringes in several successive experiments. The growth was halted by rapidly evacuating the CVD reactor from 760 Torr to below 10 mTorr in less than 3 s. Figure 8a shows an example of the growth-stop time resolved reflectivity (TRR) curves, measured at 545 °C. The top two curves correspond to the cases where the growth was stopped at the first minimum after 51 s and at the second minimum after 123 s. The furnace is then allowed to cool below 200 °C and the Si wafer was taken out of the CVD reactor, scribed, and broken at the optically monitored location. The length of the VANTAs was determined from SEM images as shown in the inset to Fig. 8a at higher magnification in Fig. 8b and c. The bottom curve in Fig. 8a represents the time evolution of the reflected intensity when the growth stops spontaneously. The first fringe (the oscillation minimum) appears when the length of the VANTAs reaches 150 ± 20 nm. The successive fringes were found to occur for constant increments in VANTA length at different growth temperatures (300 ± 30 nm at 545, 575, and 600 °C),

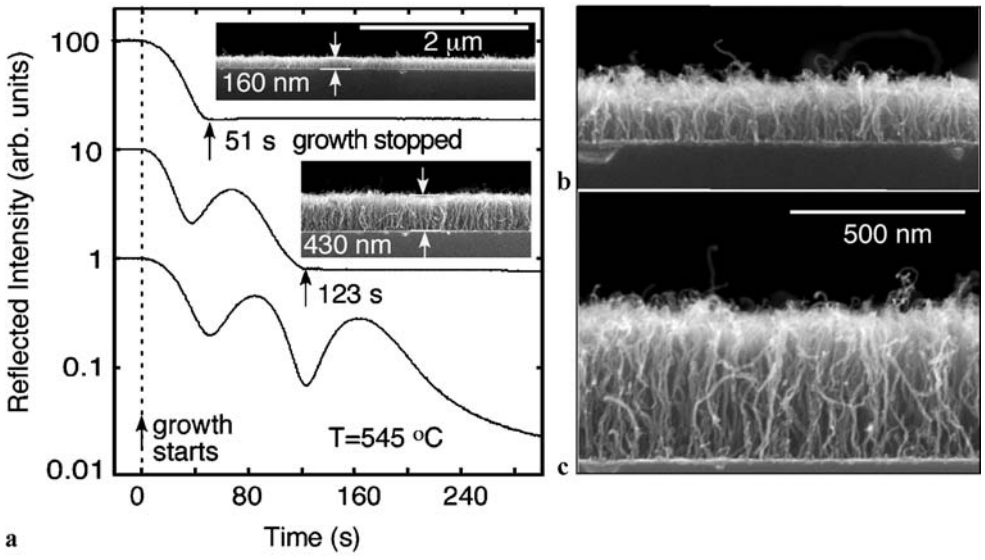

FIGURE 8 (**a**) Intensity of the specularly reflected laser beam for three different growth runs at $T = 545$ °C and 6 sccm C_2H_2. Acetylene is introduced upstream at $t = -22$ s and, after a transit time to the center of the tube furnace, growth reproducibly begins at $t = 0$ s. Attenuation of the reflected beam is accompanied by a series of interference fringes (*lower trace*). In the *top two traces* (offset for clarity), growth is stopped by rapidly evacuating the chamber just past the first and second minima at the indicated times, resulting in VANTAs of heights indicated in the corresponding cross-sectional SEM images shown in the *inset* and at higher magnification in (**b**) and (**c**)

with the uncertainty in estimating the length principally governed by the surface roughness of the VANTA. In subsequent runs, the length of the VANTAs could be directly inferred in situ by counting the fringes.

Alternatively, in the absence of pronounced Fabry–Perot fringes in the TRR signal, extinction of the laser beam can be used to estimate the length. Similar arrested growth experiments as those shown in Fig. 8 were used to estimate the extinction coefficient, $\alpha = [\ln(I_0/I)]/2d$, at each growth temperature through calibration of reflected intensity, I, and measured film thickness, d. The values of α were found to be consistent for VANTAs of different lengths at a given temperature, so the TRR signals throughout a growth run could be used to determine the VANTA length.

The standard procedure for estimating the length and growth rate is demonstrated in Fig. 9a and b. First, the times for the successive fringes (oscillation minima) were measured. Then, taking into account the measured values of the VANTA length for the first and the other successive oscillation minima, the length vs. time curve, $d(t)$, was plotted (Fig. 9b). Finally, the derivative of this curve was calculated in order to plot the growth rate vs. time (Fig. 9b). The analytical dependence, $d(t)$, required for the subsequent calculations of the shape of the oscillating reflectivity curve (Fig. 9a) was obtained using a polynomial fit to the experimental $d(t)$ points (Fig. 9b), $d(t) = 7.81t + 0.081t^2 - 0.00031t^3$, where d is in nanometers and t is in seconds.

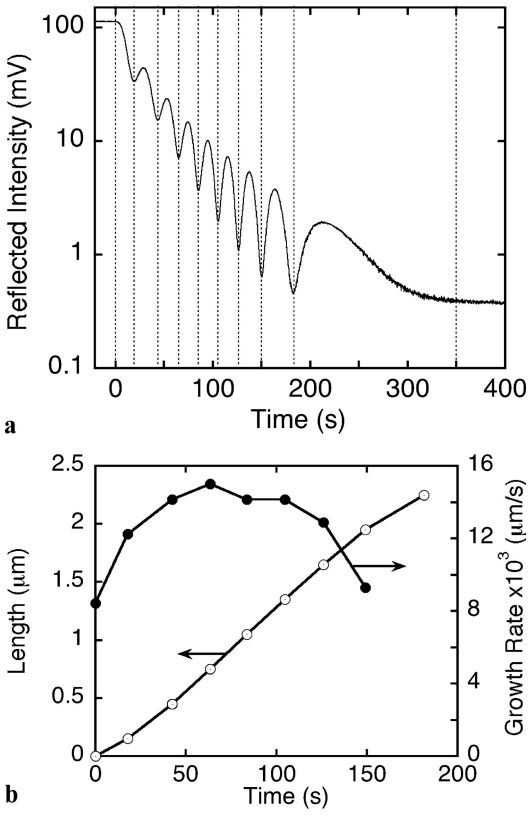

FIGURE 9 A standard procedure for estimating the VANTA length and growth rate. (**a**) Intensity of the reflected laser beam vs. growth time. C_2H_2 gas is introduced upstream at $t = -22$ s, and the growth starts at $t = 0$ s. The *vertical dotted lines* show the positions of the successive oscillation minima, which are directly related to the VANTA length. (**b**) Length of VANTAs vs. growth time and the derivative of this curve showing the time evolution of the growth rate $T = 570\,^{\circ}\mathrm{C}$

4 Calculation of reflectance and transmittance of VANTA layers

To provide a more detailed understanding of the observed interference fringes, the reflectance of a laser beam from a layer of VANTA on a Si substrate was calculated. This was done using complex refractive indices, $N = n + \mathrm{i}k$, and assuming normal incidence of the laser beam in our experimental study. The amplitude reflection and transmission coefficients ϱ_{ab} and τ_{ab} are defined by (for both s and p polarizations) [23]

$$\varrho_{ab} = \frac{N_a - N_b}{N_a + N_b}, \quad \tau_{ab} = \frac{2N_a}{N_a + N_b}, \tag{1}$$

where N_a, N_b, and N_c are the complex refractive indices of the top layer (Ar/H_2 gas), the VANTA, and the Si substrate, respectively. The reflection and transmission amplitudes, r_{ab} and t_{ab}, are given by

$$r_{ab} = \varrho_{ab} + \frac{\tau_{ab}\tau_{ba}\varrho_{bc}\Phi^2}{1 - \varrho_{bc}\varrho_{ba}\Phi^2}, \quad t_{ab} = \frac{\tau_{ab}\tau_{bc}\Phi}{1 - \varrho_{bc}\varrho_{ba}\Phi^2}, \tag{2}$$

where $\Phi = \exp(\mathrm{i}2\pi N_b d/\lambda)$. The intensity reflection coefficient can be expressed as

$$R_{ab} = r_{ab}^* r_{ab}. \tag{3}$$

Figure 10 shows the experimental TRR curve and the calculated curve using the following set of complex refractive indices: $N_a = 1$ (Ar/H_2), $N_b = 1.075 + 0.045\mathrm{i}$ (the effective refractive index for the VANTA), and $N_c = 4.1 + 0.057\mathrm{i}$ (Si, for $\lambda = 630$ nm, $T = 490\,^{\circ}\mathrm{C}$ [24]). We did not take into account the roughness of the top VANTA layer and the metal films converted to nanoparticles on the surface of the Si substrate during the pretreatment annealing. Taking into account the simplicity of the model, the calculations show a fairly

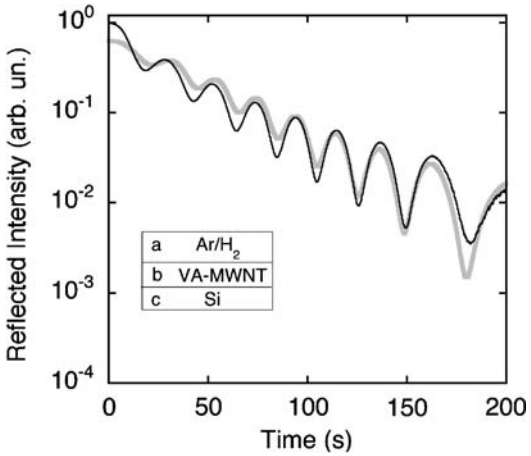

FIGURE 10 Experimental (*dark*) and calculated (*light*) TRR curves. The experimental curve is the same as shown in Fig. 9a. Three layers: (a) Ar/H_2 with the refractive index, $N_a = 1$; (b) VANTAs with the effective refractive index, $N_b = 1.075 + 0.045\mathrm{i}$; and (c) Si with $N_c = 4.1 + 0.057\mathrm{i}$, were considered in the calculations

good agreement with the experimental data except for the initial part of the curve. At the beginning, a faster decrease of the TRR signal is observed experimentally. To improve the agreement with the experimental TRR curves we considered a two-layer system, where a relatively thin layer, b2, was introduced on top of the main layer, b1. The layer b2 accounts for the slightly different properties of the top layer of the VANTA compared to the bulk VANTA. The upper layer has a relatively random set of nanotube orientations and probably contains some metal nanoparticles lifted up from the Si substrate. The TRR curve calculated using the two-layer model with a fixed value of upper-layer thickness, $d1 = 70$ nm, and $N_{b1} = 1.075 + 0.08i$, $N_{b2} = 1.075 + 0.04i$ provides a better fit to the experimental TRR curves.

Several different approaches for evaluation of the effective dielectric function of a two-phase system using the dielectric functions of its components are discussed in [23] relative to optical properties of porous silicon. Assuming that the microtopology of our VANTAs can be described using only one parameter, the porosity, p (p is the ratio of the empty pore volume to the total volume), and applying the Looyenga formula,

$$\varepsilon_{\text{eff}}^{1/3} = (1-p)\varepsilon^{1/3} + p\varepsilon_{\text{m}}^{1/3}\,, \tag{4}$$

we estimate the porosity using the dielectric function of the embedded solid phase: amorphous carbon particles $\varepsilon \sim 4$ [25], host material: gas (Ar/H_2 or air) $\varepsilon_{\text{m}} = 1$; and the calculated $\varepsilon_{\text{eff}} = n_{\text{b}}^2 = 1.16$. These assumptions give a porosity value for VANTAs of ~ 0.92.

5 Growth rates of VANTAs

In this section we describe the temperature and the C_2H_2 feedstock concentration dependences of the growth rates of VANTAs using the in situ TRR approach described above. Figure 11a and b show a set of the TRR curves for different growth temperatures. At relatively low temperatures (575–650 °C, Fig. 11a), the TRR curves show pronounced Fabry–Perot fringes in the TRR signal. When the temperature increases, the oscillation amplitudes decrease and the fringes become less pronounced. The amplitude of the TRR oscillation depends on the composition of the Fe/Mo-catalyst film, in particular on the thickness of the Mo layer. Since the thickness of the Mo layer is only 0.2 nm, it is difficult to control its thickness precisely with a standard crystal quartz balance in our electron beam evaporation chamber. Figure 11c and d show the top-layer morphology of the VANTAs at two different temperatures, 575 and 850 °C. At 850 °C the roughness of the top layer is higher than at 575 °C. Many small protruding islands (~ 1.2 μm in diameter, with a slightly larger VANTA length) are observed at higher growth temperatures. In addition, we found that at $T \geq 700$ °C the top surface of VANTAs is covered with SWNTs (see Sect. 6). This also results in an increase of the surface roughness. These two effects lead to diminishing of the TRR oscillations at high temperatures.

Figure 12a and b show the time dependence of the VANTA length for overlapping ranges of temperatures, (575–700 °C) and (700–850 °C). At 575 °C, growth continues for ~ 175 s at 0.012 μm/s. After that, growth slows down and saturates at 1.6 μm. Increasing the temperature to 600 °C results in an almost linear growth at 0.035 μm/s to 9 μm, measured after 518 s of growth time. The horizontal dotted lines show the maximum thickness of the VANTAs, measured after 518 s of growth for these two temperatures. When the temperature increases to 700 °C, the maximum achievable length also increases rapidly. For example, at 730 °C, we were able to grow VANTAs a few millimeters long. Further increase in the temperature leads to a decrease of the growth rates (Fig. 12d) and termination of growth. For example, at 800 °C and 850 °C, the maximum thickness of the VANTAs was 5.0 and 2.6 μm, respectively.

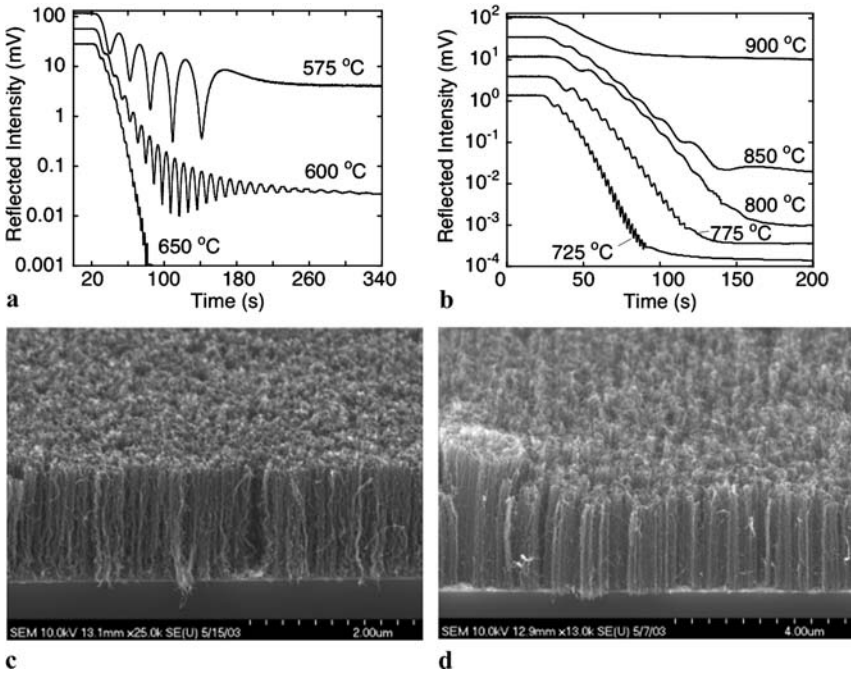

FIGURE 11 TRR curves for eight growth temperatures: (**a**) 575–650 °C and (**b**) 725–900 °C. SEM images of VANTAs at (**c**) 575 °C and (**d**) 850 °C. In all cases the VANTAs were grown in the flow of Ar (2000 sccm), H_2 (400 sccm), and C_2H_2 (6 sccm)

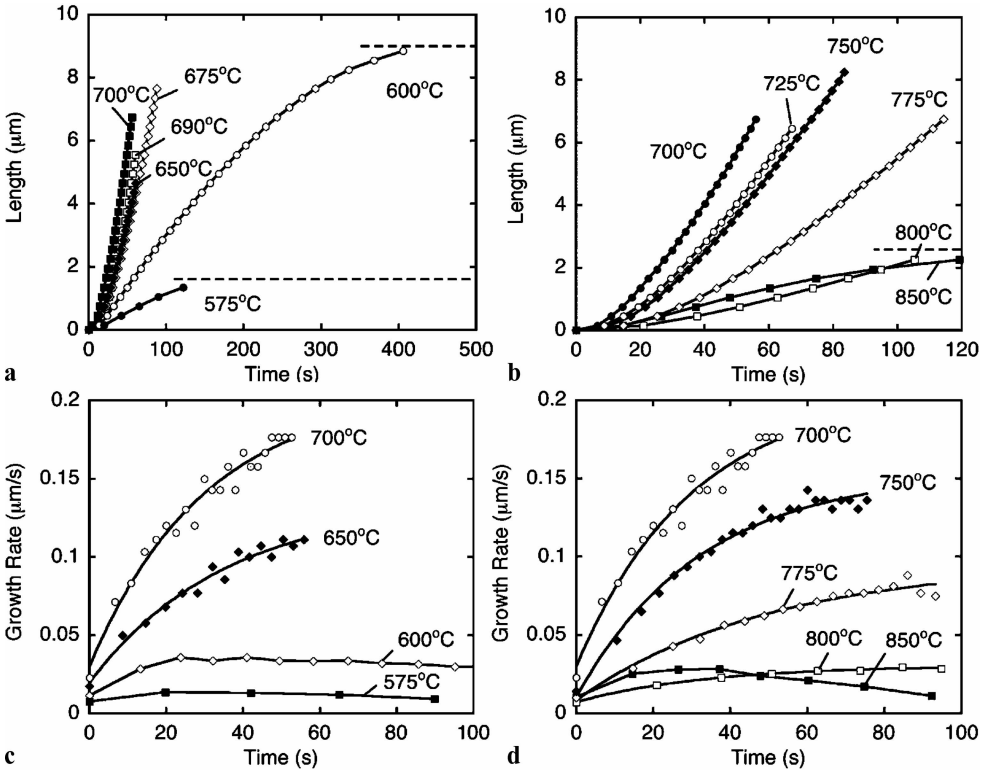

FIGURE 12 Length of VANTAs derived from the Fabry–Perot fringes shown in Fig. 11a and b for two sets of the growth temperatures: (**a**) 575–700 °C and (**b**) 700–850 °C. The *dotted horizontal lines* show the maximum achievable length of VANTAs restricted due to the termination of the growth: 1.6 μm at 575 °C, growth time 518 s; 9.0 μm at 600 °C, growth time 518 s; and 2.6 μm at 850 °C, growth time 400 s. (**c**), (**d**) Growth rates of VANTAs for the two sets of the growth temperatures calculated as a derivative from the curves shown in (**a**) and (**b**)

Another interesting feature of the growth rate vs. time curves is that at higher temperatures more time is required to reach the maximum growth rate. At 575–600 °C it takes less than 20 s to reach the maximum growth rate (Fig. 12c). At 650–700 °C, this time increases to ∼ 50 s.

Figure 13 shows the temperature dependence of the growth rates. A pronounced maximum in the growth rate of ∼ 0.2 μm/s is observed at 700 °C. The theoretical interpretation of this result using different assumptions will be presented in Sects. 7.4 and 7.5. The growth rate vs. the $1/T$ curve is nonlinear and only the low-temperature tail of this curve can be approximated by a straight line, giving an effective activation energy for the VANTA growth ∼ 2 eV. In reality, many different processes with different activation energies are involved in the growth process. A more detailed consideration of these processes will be given in Sect. 7. Interestingly, Baker et al. obtained a similar temperature dependence of the number of filaments produced per unit area and mean filament width using Co-catalyzed decomposition of acetylene [26].

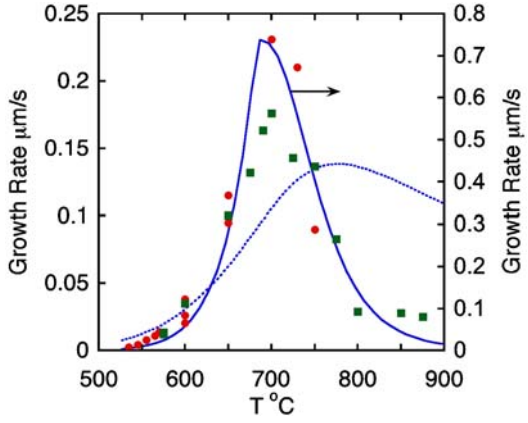

FIGURE 13 Temperature dependence of the growth rate, measured for two sets of metal catalyst films (*circles* and *squares*), consisting of 10 nm Al, 1 nm Fe, and 0.2 nm Mo, but deposited at different runs which can be slightly different in nominal film thickness due to difficulties in controlling the film thickness with Angstrom precision. The *solid* and *dashed lines* show the calculated temperature dependences assuming different mechanisms of catalyst deactivation at higher temperatures: poisoning of catalyst nanoparticles due to gas-phase pyrolysis products (Sect. 7.4) and reducing of active catalyst state (Sect. 7.5), respectively

In the absence of pronounced Fabry–Perot fringes in the TRR signal, the length was estimated from extinction of the laser beam. This procedure is described in Sect. 4 and [6]. The extinction coefficients decrease approximately by a factor of three in the temperature range from 600 °C to 750 °C (see [6]). While porosity of the VANTAs is difficult to quantify, it did not appear to vary sufficiently to explain the decrease. A more likely explanation is the pronounced decrease in the number of walls of the CNTs grown with increasing temperature. As shown in Fig. 14a, b, and c, high-resolution TEM images reveal that thicker, more defective MWNTs with 6–10 walls are grown at 575 °C while cleaner, predominantly double-walled nanotubes (DWNTs) can be found in VANTAs (Fig. 14d) grown at 725 °C. In addition the TEM images show some SWNTs in VANTAs grown at 725 °C (Fig. 14c).

Figure 15a–c show the dependence of the growth rates on concentration of C_2H_2 feedstock gas measured at 575 °C. The maximum growth rate remains practically constant in the C_2H_2 flow-rate range from 2 to 19 sccm (Fig. 15b). The most interesting and important result is that the terminal length of the VANTAs can be substantially increased by decreasing the feedstock gas concentration (Fig. 15c). The discussion and theoretical interpretation of these results will be presented in Sect. 7.

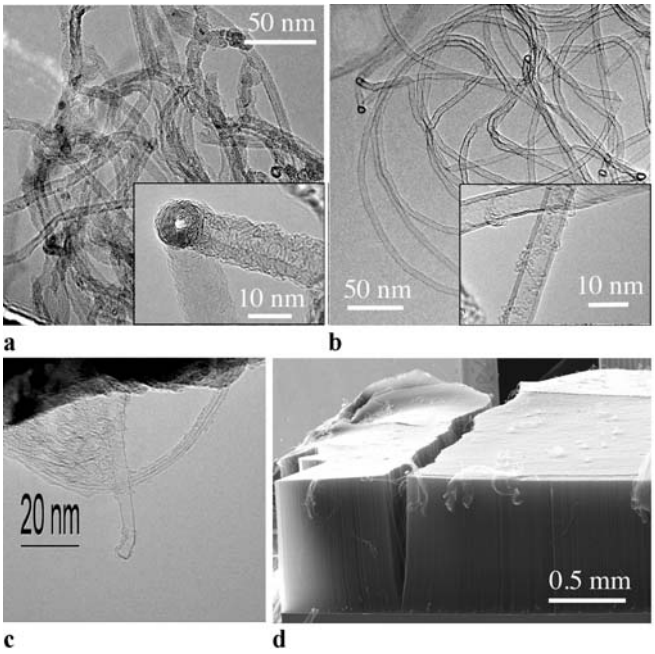

FIGURE 14 TEM images of multi-walled carbon nanotubes grown from metal multi-layered catalyst films at (**a**) 575 °C, (**b**) 725 °C, and (**c**) 725 °C. (**d**) SEM image of 0.75-mm-long VANTAs grown at 730 °C

6 Raman spectra of carbon nanotubes

Figure 16 shows a set of Raman spectra of carbon nanotubes grown at different temperatures. In the temperature range 550–650 °C, the tangential mode contains two relatively intense peaks at 1600 cm^{-1} (*G*-band) and 1320 cm^{-1} (*D*-band) (Fig. 16a). We did not observe any features specific to SWNTs in the low-frequency region at these temperatures (Fig. 16b). The low-frequency spectrum measured at 550 °C, when the thickness of the VANTA array is only $\sim 1.2\,\mu m$ and the VANTA layer is transparent to 632.8-nm excitation laser light, shows a characteristic wing in the frequency range $\sim$ 220–300 nm. This wing comes from the 303-cm^{-1} band of the supporting Si substrate. At 700 °C, the shape and the D/G peak intensity ratio change and a very pronounced peak appears around 180 cm^{-1} in the breathing mode region. These changes indicate the sudden appearance of SWNTs/DWNTs in the samples of VANTAs. At higher growth temperatures (700–900 °C), the Raman spectra in the tangential (Fig. 16c) and breathing (Fig. 16d) mode regions show strong features of SWNTs/DWNTs. The Raman spectra are in good agreement with the high-resolution TEM imaging studies.

7 Kinetic model of VANTA growth

In this section we discuss the main processes that could be responsible for the effects observed in the VANTA growth using our in situ diagnostic techniques. To understand the observed growth dependences we developed a model based on kinetic equations that describes the catalytic conversion of the feedstock gas into carbon nanotubes. Since the growth of CNTs contains numerous unknown microscopic mechanisms, we consider a few dominant mechanisms and compare calculated and experimental kinetics to support or eliminate any specific mechanism based on this comparison. Ideally the model should explain: the measured VANTA lengths and their time evolution during growth, the observed growth rates, the temperature dependence of the growth rates, the growth termination at low and high temperatures, the feedstock partial pressure dependence of the growth rate, and the observed change in the type of carbon nanotubes pro-

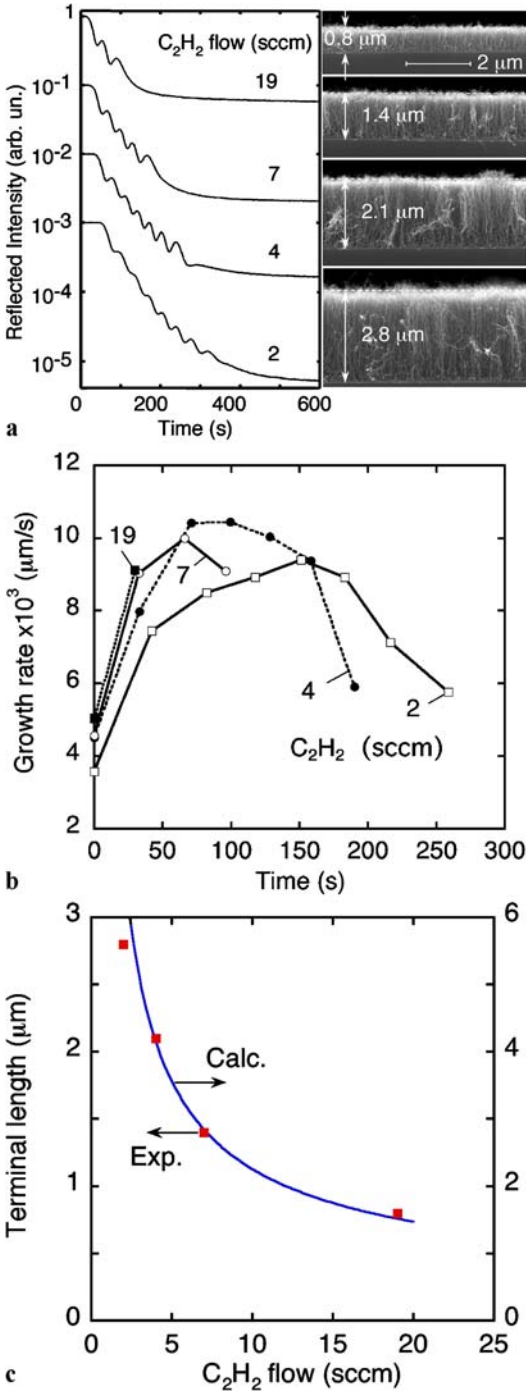

FIGURE 15 (**a**) TRR curves for four different flow rates of C_2H_2 feedstock gas measured at the growth temperature of 575 °C (*left*) and SEM images of the corresponding arrays showing the increase of the terminal length from 0.8 μm to 2.8 μm as the acetylene flow rate drops from 19 to 2 sccm (*right*). (**b**) Growth rate vs. time curves derived from the TRR curves shown in (**a**). (**c**) Terminal length of VANTAs vs. C_2H_2 flow rate (*squares*). The *solid line* represents the results of calculations described in Sect. 7.5

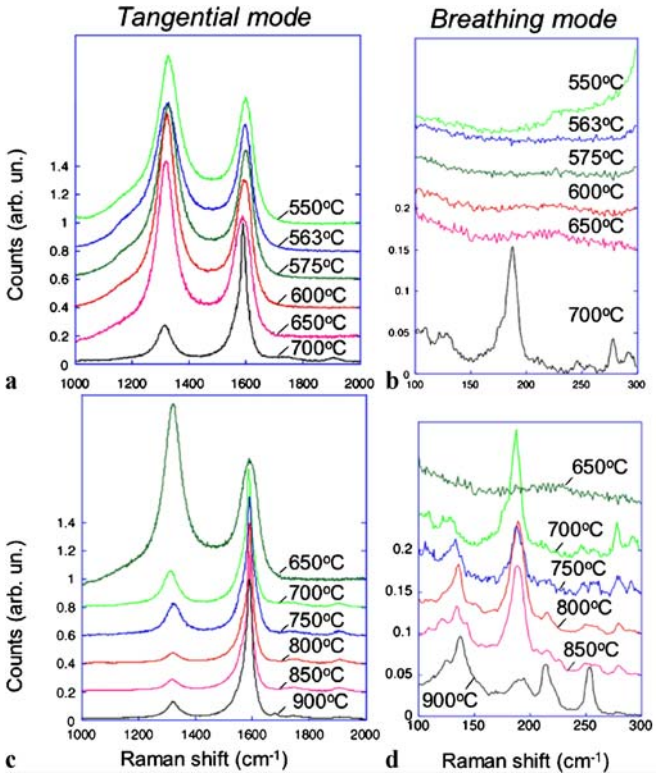

FIGURE 16 Raman spectra of carbon nanotubes grown at different temperatures: (**a**), (**b**) 550–700 °C and (**c**), (**d**) 650–900 °C

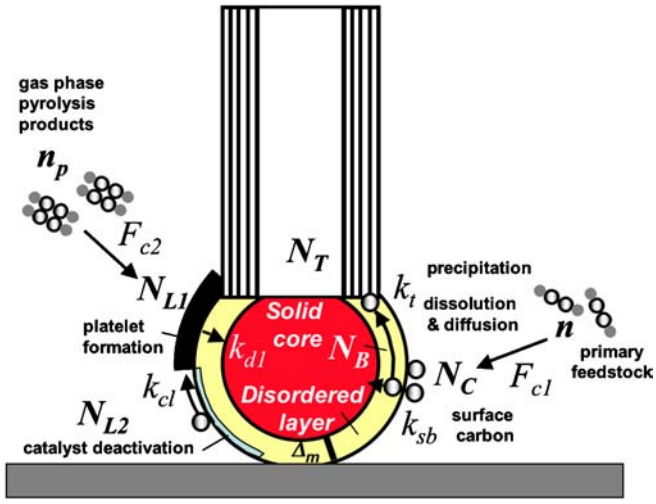

FIGURE 17 Schematic representation of processes responsible for feeding and termination of carbon nanotube growth: (1) impingement of C_2H_2 molecules into the catalyst particle surface; (2) chemisorption and catalytic decomposition of C_2H_2 molecules on the surface of the catalyst particle; (3) surface–bulk penetration of carbon atoms with the rate constant, k_{sb}; (4) formation of disordered surface layer with thickness Δ_m; (5) diffusion of carbon atoms channeled by the disordered layer; (6) precipitation of carbon species into a nanotube with the rate constant, k_t; (7) formation of carbonaceous layer defined by rate constant, k_s, that finally stops the decomposition of C_2H_2 and terminates the growth; (8) gas-phase decomposition of C_2H_2 and formation of pyrolysis products in the gas phase; (9) impingement of the pyrolysis products into the catalyst particle surface; (10) additional growth of the carbonaceous layer due to gas-phase pyrolysis products; (11) catalyst deactivation, e.g. due to oxygen reduction at higher temperatures and formation of inactive layer

duced when the temperature increases, i.e. transition from MWNTs to DWNTs/SWNTs. In addition, the growth model should also explain: the role of the metal catalyst nanoparticles in VANTA growth, the optimal size and composition of the catalyst nanoparticles for fast growth of long and dense VANTAs, a mechanism and efficiency of the catalytic decomposition of feedstock molecules, dissolution and diffusion of carbon atoms/molecules through the metal nanoparticles, the phase state of the catalyst nanoparticles during nanotube nucleation and growth, and precipitation of the carbon atoms/molecules and nanotube nucleation resulting in different nanotube types, i.e. different diameters and numbers of walls. Many of these processes have been discussed in the literature, basically inspired by the early work by Baker et al. [3, 26, 27] (see also [28]). A detailed theoretical discussion of VANTA growth has been given in [29, 30].

7.1 *The main processes*

Figure 17 summarizes the processes we had taken into account in our attempt to explain the observed kinetics of the VANTA growth. Initially C_2H_2 feedstock molecules at concentration n collide with the surface of a catalyst nanoparticle providing a constant flux of carbon-containing molecules, F_{c1}, to the surface of the catalyst nanoparticle. A small fraction of these molecules bonds to the nanoparticle surface due to chemisorption and catalytically decomposes, producing the starting source of carbon atoms, N_C, for CNT growth.

The adsorption and decomposition of acetylene on different Fe facets have been studied experimentally [31] and theoretically [32]. It was shown that during decomposition of acetylene strong hybridization between C and Fe atoms leads to weakening of the C−H and C−C bonds followed by formation of two CH radicals or CCH and H radicals, and finally dissociation into isolated C and H atoms [32].

We assume further that dissolution of carbon atoms with the rate constant, k_{sb}, forms a highly disordered 'molten' layer on the surface of the catalyst nanoparticle. The thickness, Δ_m, of this layer is defined by the maximum number of the feedstock molecules decomposed on the surface of the catalyst nanoparticle, N_C, for a particular temperature. This layer channels diffusion of the dissolved carbon atoms, N_B, with a rate constant k_t and their precipitation into a nanotube because of much higher carbon diffusivity in the disordered layer compared to the ordered solid phase. For example, in the disordered liquid iron phase the diffusion coefficient of carbon atoms, D_L, is about $(1–5)\times10^{-5}$ cm^2/s at $T = 1000$ K, which is almost three orders of magnitude higher compared to that in the solid phase, $D_S \approx 10^{-8}$ cm^2/s at $T = 1000$ K [33]. The thickness of the disordered layer, Δ_m, expressed in the number of carbon monolayers defines the number of CNT walls. The surface melting of small particles, i.e. formation of the liquid skin below their melting temperatures, was studied theoretically and experimentally for different nanoparticles including Fe_xC_y clusters (see for example [34] and references therein).

Although the majority of the carbon atoms follows this kinetic path and feeds the CNT growth, a relatively small fraction of these atoms forms a carbonaceous layer on the surface of the catalyst nanoparticle. This carbonaceous layer

decreases the nanoparticle surface area available for catalytic decomposition of the incoming feedstock molecules; thus, it restricts the source flux of carbon atoms available for the CNT growth. Finally, when the whole surface of the catalyst nanoparticle is covered with the carbonaceous layer, the carbon source terminates and the growth stops. The carbonaceous layer, presented as a 'platelet' in Fig. 17, is shown only to simplify the schematic. In reality, island-like nucleation and growth of the carbonaceous layer containing N_{L1} carbon atoms takes place, with the overall rate constant, k_{cl}. As will be shown later, this set of simple assumptions describes quite well the observed growth kinetics and the terminal length of VANTAs measured at relatively low temperatures (535–700 °C).

To account for the high-temperature (700–900 °C) kinetics and the terminal lengths of VANTAs we have to introduce additional mechanisms that are responsible for the catalytic activity of the catalyst nanoparticles at higher temperatures. Basically, any process that leads to temperature-induced deactivation of the catalyst nanoparticles, e.g. poisoning due to gas-phase pyrolysis products [35]; formation of iron carbide, Fe_3C, as was suggested in [26]; any change in the oxidation state of the Fe/Mo catalyst, e.g. due to direct oxygen desorption at the higher temperatures or indirect hydrogen-induced reduction; diffusion of Si atoms from a Si substrate into the catalyst nanoparticle, etc., could contribute to catalyst deactivation at higher temperatures. Some of these mechanisms have specific intrinsic kinetics that could lead to different overall fits to the observed growth kinetics. This provides a way for assessing the role of specific processes responsible for growth at the higher temperatures. Therefore, initially we consider some of these processes using a general kinetic description trying to avoid complicated and poorly understood chemistry behind these specific mechanisms.

First, we consider the additional carbon flux, F_{c2}, which contributes to the formation of the poisoning carbonaceous layer, N_{L1}, due to gas-phase pyrolysis products, n_p, of the feedstock molecules (C_2H_2). This layer could be partially dissolved by the catalyst nanoparticle that is described by the dissolution rate constant, k_{d1}. Second, we introduce an additional effective inactive catalyst layer, N_{L2}, which forms due to additional mechanisms discussed above. The deactivated layer could also be reactivated, for example by introducing water [35] or other catalyst activation gases into the CVD reactor, which can be described by the activation rate constant, k_{d2}. It should be mentioned that the inactive layer in Fig. 17 is shown to simplify the schematic. In reality, deactivation of the catalyst occurs randomly throughout the surface of the catalyst nanoparticle.

7.2 *Kinetic equations*

The processes discussed above can be described by the following set of differential equations:

$$\frac{dN_C}{dt} = \tilde{F}_{c1} n \left(1 - \frac{N_L}{\alpha S_0 n_m}\right) - (k_{sb} + k_{cl})\, N_C \,, \tag{5a}$$

$$\frac{dN_{L1}}{dt} = \tilde{F}_{c2} n_p \left(1 - \frac{N_L}{\alpha S_0 n_m}\right) + k_{cl} N_C - k_{d1} N_{L1} \,, \tag{5b}$$

$$\frac{dN_{L2}}{dt} = K_r \left(1 - \frac{N_L}{\alpha S_0 n_m}\right) - k_{d2} N_{L2} \,, \tag{5c}$$

$$\frac{dN_B}{dt} = k_{sb} N_C - k_t N_B + k_{d1} N_{L1} \,, \tag{5d}$$

$$\frac{dN_T}{dt} = k_t N_B \,, \tag{5e}$$

$$\frac{dn_p}{dt} = k_{1p} n^2 - k_{2p} n_p \,, \quad n + 2n_p = \tilde{n}_0 \,, \tag{5f}$$

$$N_L = N_{L1} + N_{L2} \,, \tag{5g}$$

where N_C is the number of carbon atoms on the surface of the catalyst nanoparticle produced by catalytic decomposition of the feedstock molecules, C_2H_2; N_{L1} and N_{L2} are the numbers of carbon atoms converted to the carbonaceous layer on the nanoparticle surface and inactive catalyst atoms on the surface of the catalyst nanoparticle, respectively; N_B is the number of carbon atoms diffused into the catalyst nanoparticle; N_T is the number of carbon atoms precipitated into a nanotube; $n_m = 10^{15}$ atoms/cm^2 is the surface density of a monolayer of carbon atoms, α is the number of monolayers, and S_0 is the nanoparticle surface area; $\tilde{F}_{c1} = F_{c1}/n$, $\tilde{F}_{c2} = F_{c2}/n_p$, and $\tilde{n}_0 = g(t) n_0$, where $g(t)$ is the factor describing the leading edge of the gas front at the substrate position in the furnace.

The fluxes F_{c1} and F_{c2} can be estimated as

$$F_{c1} = F_{b1} p_1 \exp\left(-\frac{E_{a1}}{k_B T}\right) \,, \quad F_{c2} = F_{b2} p_2 \exp\left(-\frac{E_{a2}}{k_B T}\right) \,, \tag{6}$$

where p_1, p_2 are the pre-exponential factors, and E_{a1}, E_{a2} are the activation barriers for sticking and catalytic decomposition of the feedstock molecules and their gas-phase products, respectively. Here F_{b1} and F_{b2} are the fluxes of the carbon feedstock gas (C_2H_2) and its main pyrolysis product on the surface of a metal catalyst nanoparticle, respectively:

$$F_{b1} = \frac{1}{4} S_0 n \left(\frac{k_B T}{2\pi m}\right)^{1/2} \,, \quad F_{b2} = \frac{1}{4} S_0 n_p \left(\frac{k_B T}{2\pi M}\right)^{1/2} \,, \tag{7}$$

where $S_0 = 4\pi R^2$, R is the nanoparticle radius, n, n_p are the partial densities of C_2H_2 and its main pyrolysis product in the flowing $Ar/H_2/C_2H_2$ gas mixture, k_B is the Boltzmann constant, T is the gas temperature, and m, M are the masses of a C_2H_2 molecule and its major pyrolysis product, respectively. For example, for a catalyst particle of $R = 5$ nm, $F_{b1} \approx 1.1 \times 10^9$ molecules/s and $F_{c1} \approx 3 \times 10^5$ atoms/s at 575 °C, 2 Torr C_2H_2 partial pressure, $E_{a1} = 0.6$ eV, and $p_1 = 1$.

In this model we consider the simplest case when the dimers, C_4H_4, form the flux, F_{b2}, with the density, $n_p = (n_0 - n)/2$, where n_0 is the initial partial density of C_2H_2 molecules. Equation (5f) describes formation of the dimers in the gas phase with the direct and reverse rate constants k_{1p} and k_{2p}, respectively. In the case when $n_p \ll \tilde{n}_0$, we have $n_p \approx (k_{1p}/k_{2p})\,(\tilde{n}_0)^2$, where $k_{1p}/k_{2p} = P \exp\left(-E_p/k_B T\right)$, P is a pre-exponential factor, and E_p is the activation barrier for gas-phase decomposition of the feedstock gas. We assume that the pyrolysis products decompose only partially on the surface of the catalyst nanoparticle and supply carbon directly to the carbonaceous layer, N_{L1}.

The rate constants, k_{sb} and k_{cl}, describe surface–bulk penetration and formation of the carbonaceous layer, respectively:

$$k_{sb} = B \exp\left(-\frac{E_{sb}}{k_B T}\right), \quad k_{cl} = A \exp\left(-\frac{E_{cl}}{k_B T}\right), \tag{8}$$

where E_{cl}, E_{sb} are the activation barriers for the carbonaceous layer formation and surface–bulk penetration of carbon atoms, respectively, and A, B are pre-exponential factors. The characteristic rate constant for the bulk diffusion to the growth edge of a carbon nanotube can be estimated as

$$k_t = \left(\frac{D_0}{R^2}\right) \exp\left(-\frac{E_b}{k_B T}\right), \tag{9}$$

where $D_0 \sim 0.1$–$0.5\ \mathrm{cm}^2/\mathrm{s}$ and $E_b \sim 1.4$–1.6 eV, for the temperatures $T = 1000$–1500 K [29].

The rate constant, K_r, in (5c) has a different meaning depending on the specific process responsible for the catalyst deactivation. For example, in the case of direct oxygen desorption from the surface of the catalyst nanoparticle at higher temperatures, $K_r = M_1 \exp(-E_{r1}/k_B T)$. In the case of reduction of the active catalyst oxidation state due to H_2 in the gas flow, $K_r = \tilde{F}_{H_2} n_{H_2} k_{r2}$, where $\tilde{F}_{H_2} n_{H_2}$ is the hydrogen flux onto the surface of the catalyst nanoparticle and $k_{r2} = M_2 \exp(-E_{r2}/k_B T)$ is the corresponding rate constant for sticking and dissociation of H_2 on the surface of the catalyst nanoparticle.

The number of CNT walls is defined by the thickness of the disordered layer, Δ_m, expressed as the number of carbon monolayers: $N_w = \max(N_C)/\tilde{\alpha} S_0 n_m$ if $N_w > 1$, and $N_w = 1$ if $\max(N_C)/\tilde{\alpha} S_0 n_m \le 1$, where $\tilde{\alpha}$ is an adjustable parameter.

7.3 *A simplified model: analytical solution of the rate equations*

To understand what parameters in the rate equations (5a)–(5g) control the growth kinetics and termination, and also to provide a basis for choosing appropriate rate constants for numerical solution of (5a)–(5g), we consider first the analytical solution of these equations in the simplified case where we neglect the gas-phase pyrolysis of the feedstock, i.e. the first terms in (5b) and (5f) as well as the additional catalyst deactivation step described by (5c). Using these assumptions, we are basically neglecting all the processes that describe CNT growth at higher temperatures ($> 700\,^\circ$C).

In addition, we assume that $g(t) = 1$, and that the dissolution of the carbonaceous layer on the surface of the carbon nanoparticle could be neglected, i.e. $k_{dl} \ll k_{sb}, k_{cl}, k_t$. Also, we assume that the number of the CNT walls remains constant, so the length, L, of the CNT arrays could be estimated as $L = N_t/z$, where z is the number of carbon atoms per one micron of nanotube length. For a 10-wall nanotube of $R = 5$ nm, one can estimate z as $\sim 7 \times 10^6$ atoms/μm. In this case the time evolution of the carbon nanotube length, $L(t)$, can be described by

$$\begin{aligned} L(t) = N_T/z = {} & \\ & K k_t \left[\frac{1}{\gamma_2 (k_t - \gamma_2)} \exp(-\gamma_2 t) - \frac{1}{\gamma_1 (k_t - \gamma_1)} \exp(-\gamma_1 t) \right. \\ & \left. + \frac{1}{k_t (k_t - \gamma_1)} \exp(-k_t t) - \frac{1}{k_t (k_t - \gamma_2)} \exp(-k_t t) \right] \\ & + K \left(\frac{\gamma_2 - \gamma_1}{\gamma_1 \gamma_2} \right), \end{aligned} \tag{10}$$

where $K = F_{c1} k_{sb}/2Dz$, $\gamma_1 = (m_1/2) - D$, $\gamma_2 = (m_1/2) + D$, $D = \sqrt{(m_1^2/4) - m_2}$, $m_1 = k_{cl} + k_{sb}$, and $m_2 = F_{c1} k_{cl}/\alpha S_0 n_m$.

In the case when $k_{sb} \ll k_{cl}$, one can obtain

$$\begin{aligned} L(t) \approx \frac{F_{c1}}{z} & \left[\frac{k_{sb} \alpha S_0 n_m}{k_{cl} F_{c1}} \left(1 - \exp\left(-\frac{F_{c1} k_{cl}}{\alpha S_0 n_m k_{sb}} t \right) \right) \right. \\ & \left. - \frac{k_{sb}}{k_t (k_t - k_{sb})} \exp(-k_t t) + \frac{k_t}{k_{sb} (k_t - k_{sb})} \exp(-k_{sb} t) \right]. \end{aligned} \tag{11}$$

Equation (11) shows that the growth kinetics is defined by three exponential terms and can be analyzed using two considerably different time scales. The relatively fast kinetics are defined by the last two terms in (11) and have the characteristic times, $\tau_t = 1/k_t$ and $\tau_{sb} = 1/k_{sb}$, which can be estimated as $\tau_t \approx 6 \times 10^{-5}$ s and $\tau_{sb} \approx 1.2 \times 10^{-3}$ s at $T = 700\,^\circ$C. Here we assume that $D_0 = 0.25\ \mathrm{cm}^2/\mathrm{s}$ and $E_{sb} = 2.2$ eV. These times are much smaller than the time resolution of our reflectivity detection system (~ 0.14 s) and the corresponding kinetics cannot be resolved in the experimental $L(t)$ curves. The first term in (11) basically defines the relatively slow process of the growth termination with the characteristic termination time and length

$$\tau_{term} \approx \frac{\alpha S_0 n_m}{F_{c1}} \frac{k_{sb}}{k_{cl}}, \quad L_{term} \approx \frac{\alpha S_0 n_m}{z} \frac{k_{sb}}{k_{cl}}. \tag{12}$$

This means that both the termination time and length are defined by the ratio of the surface–bulk penetration and carbonaceous layer formation rate constants (8). From (12) it is also clear that the termination length exponentially depends on $1/T$, i.e. $L_{term} \propto \exp[-(E_{sb} - E_{cl})/k_B T]$. Depending on the value of k_{cl}, which will be determined later by fitting the experimental data, the characteristic growth time can exceed 10^3 s. The value of E_{sb} can be simply estimated by fitting the experimental $L_{term}(T)$ curves measured at low temperatures, assuming that $E_{cl} = 0$.

The analytical solution of the simplified rate equations describes the experimental growth kinetics and explains the observed exponential dependence of the terminal length on $1/T$ at low growth temperatures ($< 700\,^\circ$C).

7.4 *Poisoning of catalyst nanoparticles by gas-phase pyrolysis products*

Poisoning of catalyst nanoparticles by gas-phase pyrolysis products is a common assumption that is used frequently to explain growth termination of carbon nanotubes (see for example [35]). To explore this assumption as an additional mechanism for CNT growth termination, we included it in the kinetic equations (5).

Initially we introduce acetylene in the cold zone of the quartz tube (Fig. 1). When it reaches the hot zone, where a Si substrate covered with a catalyst nanoparticle layer is located,

acetylene can be partially decomposed due to gas-phase pyrolysis. At the temperatures used in this study (530–900 °C) only a small fraction ($\sim 10^{-4}$) of the original feedstock gas decomposes and forms pyrolysis products in the gas phase. Despite a relatively small fraction of the C_2H_2 molecules decomposed in the gas phase, it is important to consider this process, since these products accumulate on the surface and contribute to the long time growth kinetics especially at higher growth temperatures.

At high temperatures, C_2H_2 effectively decomposes in the gas phase that results in formation of polycyclic aromatic hydrocarbon molecules (PAH). The experimental studies of gas-phase pyrolysis of C_2H_2 molecules in the temperature range ~ 350–3100 °C were summarized by Tanzawa et al. [36]. In the low-temperature range the chain reaction involving a hydrogen atom is responsible for the initial decomposition through the reactions $H + C_2H_2 \rightarrow C_2H_3$, $C_2H_3 + C_2H_2 \rightarrow C_4H_4 + H$, etc. The initial H atoms can be produced by the reaction $C_2H_2 + C_2H_2 \rightarrow C_4H_3 + H$ having an activation energy of ~ 2 eV. It should be mentioned that the direct dissociation channel of the C_2H_2 molecule, $C_2H_2 + M \rightarrow C_2H + H + M$, requires the activation energy of ~ 4.6 eV and is almost negligible at low temperatures. Different mechanisms of aromatic structure (PAH) formation and eventually soot formation in gas-phase C_2H_2 pyrolysis were considered by Frenklach et al. [37].

To account for the gas-phase pyrolysis products, we consider the simplest case of gas-phase dimer formation (5f) and their chemisorption (5b) on the surface of the catalyst nanoparticle. In these calculations we neglect (5c), which describes deactivation of the catalyst nanoparticle at higher temperatures.

Another important factor that contributes to the growth kinetics is the feedstock gas introduction front, $g(t)$, which defines the shape of the leading edge of the acetylene gas flow. In the case of our experimental geometry, this factor is defined by the characteristic time of about 25 s required for the feedstock gas to reach the Si substrate, as well as by carrier gas flow and pressure. Because of the relatively complex transient gas flow pattern forming during acetylene introduction into the stationary flowing Ar/H_2 gas, it is hard to calculate the temporal shape of the feedstock gas leading edge. Therefore, in our further numerical calculations we assume that $g(t) = 1 - \exp(-\kappa t)$, where the feedstock gas leading edge sharpness parameter κ will be defined by fitting the experimental $L(t)$ curves.

Figure 18a and b show the calculated time dependences of VANTA length at different temperatures. For this case we assumed that $p = 1$, $\alpha = 1$, $R = 5$ nm, $n_0 = 6.6 \times 10^{16}$ 1/cm^3, $E_{a1} = E_{a2} = 0.6$ eV, $E_b = 1.5$ eV, $E_{sb} = 2.2$ eV, $k_{sb} = 17$ s^{-1} at $T = 575$ °C, $E_{cl} = 0$, $k_{cl} = 3 \times 10^{-3}$ s^{-1}, $k_t = 491$ s^{-1} at 575 °C, $E_p = 2.6$ eV, $\kappa = 0.02$ s^{-1}, and that the dissolution of the carbon layer on the surface of the carbon nanoparticle could be neglected, i.e. $k_{d1} \ll k_s, k_{sb}, k_t$. The calculated curves (Fig. 18a) describe fairly well the experimental dependences of VANTA length vs. growth time (Fig. 12a) assuming slightly different temperatures.

Figure 19 demonstrates the experimental and calculated temperature dependences of the terminal length assuming $E_{sb} = 2.2$ eV and $E_p = 2.6$ eV (dashed curve). The terminal length increases rapidly when the temperature increases, reaches a maximum around 700 °C, and drops again at higher temperatures. According to this model, the temperature behavior of the terminal length is defined by two competing processes, activation of the catalyst nanoparticle related to the

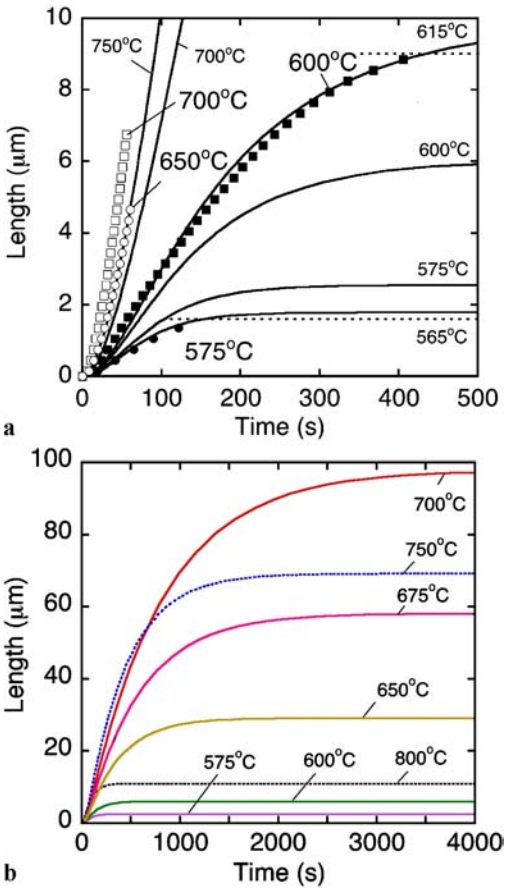

FIGURE 18 (**a**) Calculated (*lines*) and experimental (*dots*) dependences of VANTA length vs. growth time at different temperatures in the ranges 575–700 °C and (**b**) 700–900 °C

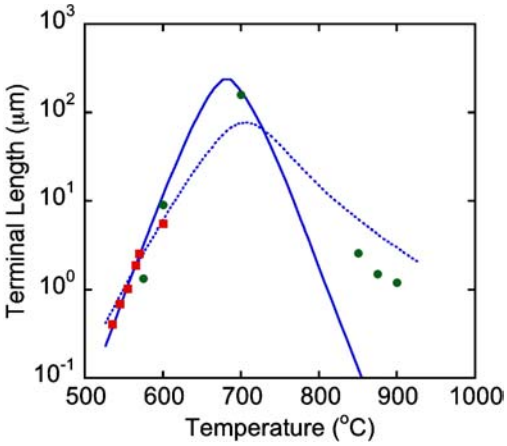

FIGURE 19 Experimental (*dots*) and calculated (*lines*) dependences of the terminal length of VANTAs on growth temperature. The terminal lengths were measured directly using SEM. The *lines* show the calculated temperature dependences assuming different mechanisms of catalyst deactivation at higher temperatures: (1) poisoning of catalyst nanoparticles due to gas -phase pyrolysis products (*dashed line*, see Sect. 7.4) and (2) reducing of the active catalyst state (*solid line*, see Sect. 7.5)

activation barrier, E_{sb}, and deactivation of its catalytic activity in this particular case due to additional poisoning by acetylene gas-phase pyrolysis products having the formation activation energy, E_p.

The observed temperature dependence of the growth rate (Fig. 13, dashed curve) shows the same type of behavior as $L_{term}(T)$, i.e. a maximum around 700 °C with a rapid fall at lower and higher temperatures. Although the considered model describes this behavior well qualitatively, it does not provide a good quantitative description of the growth-rate data, especially at $T \geq 700$ °C.

The calculated dependences of the maximum length of VANTAs vs. acetylene flow reveal additional problems with our initial assumptions. The experimental dependence measured at 575 °C (Fig. 15c) clearly shows an increase in the terminal length when the partial pressure (flow) of C_2H_2 drops. Although the calculated dependences (Fig. 20) show a similar behavior at higher temperatures, they exhibit a constant pressure dependence at all temperatures below 650 °C.

These discrepancies suggest that poisoning of the catalyst nanoparticles by gas-phase decomposition products is not the major process that is responsible for the catalyst deactivation at higher growth temperatures.

7.5 *Deactivation of catalyst nanoparticles during CNT growth*

In this section we consider an alternative description of deactivation of the catalyst nanoparticle using (5c) and neglecting the first term in (5b), which describes catalyst poisoning due to gas-phase pyrolysis products.

The result of calculations of the maximum growth rate vs. temperature based on these kinetic equations (5) is shown in Fig. 13 by the solid line. In these calculations we assumed that $M = 1.2 \times 10^8$, $E_r = 2.4$ eV, and $\tilde{\alpha} = 0.3$. Here the parameter $\tilde{\alpha}$ was adjusted to fit the average number of walls, $N_w \approx 10$, measured experimentally at $T = 575$ °C using high-resolution TEM. The modified kinetic model provides a better fit to the experimental growth rates compared to the kinetics based on catalyst deactivation by gas-phase pyrolysis products (Fig. 13, dashed curve). It should be mentioned that the absolute value of the calculated growth rate is higher than that observed experimentally, which could be explained by the wiggly shape of CNTs in vertically aligned arrays. The wiggling will result in an increase of the actual length of the tubes compared to that measured experimentally as the length of VANTAs.

The modified kinetics also describes fairly well the dependence of the terminal length vs. temperature as shown by the solid line in Fig. 19, although some discrepancy is observed at the high temperatures. Figure 21 shows the terminal length vs. temperature plot calculated at different flow rates (partial pressures) of C_2H_2. The maximum terminal length slightly shifts to lower temperatures as C_2H_2 flow decreases from 20 to 2 sccm. Interestingly, the previous version of the model which includes catalyst poisoning due to gas-phase pyrolysis products predicts an opposite trend, i.e. a relatively large shift of the terminal length maximum to high temperatures occurs when C_2H_2 flow increases (Fig. 22). This kind of parametric calculation provides a clear route for choosing between different mechanisms of catalyst deactivation at the higher temperatures.

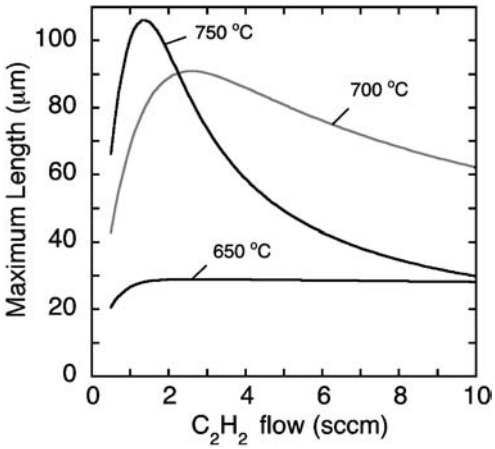

FIGURE 20 Calculated dependences of the maximum length vs. acetylene flow rates at different temperatures: 650, 700, and 750 °C

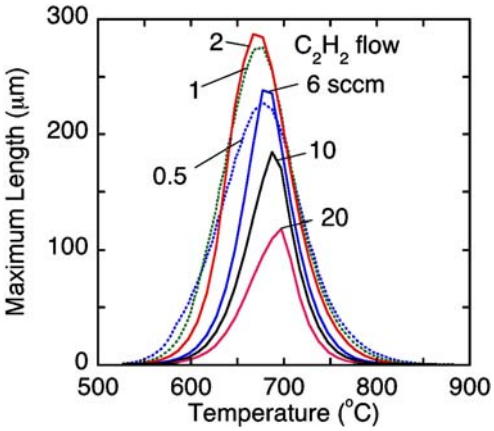

FIGURE 21 Calculated dependences of the terminal length vs. temperature at different acetylene flow rates in the range 0.5–20 sccm

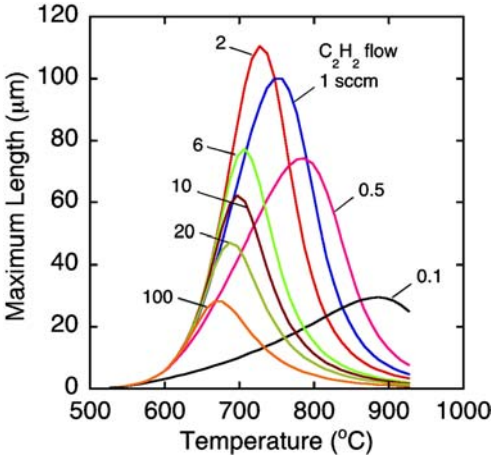

FIGURE 22 Calculated dependences of the terminal length vs. temperature at different acetylene flow rates in the range 0.1–100 sccm

The dependence of the maximum growth rate vs. temperature calculated at different C_2H_2 flow rates (Fig. 23) shows that the maximum growth rate increases as C_2H_2 flow increases. The open circles indicate the points when the number of nanotube walls approaches 1. One can see that SWNTs

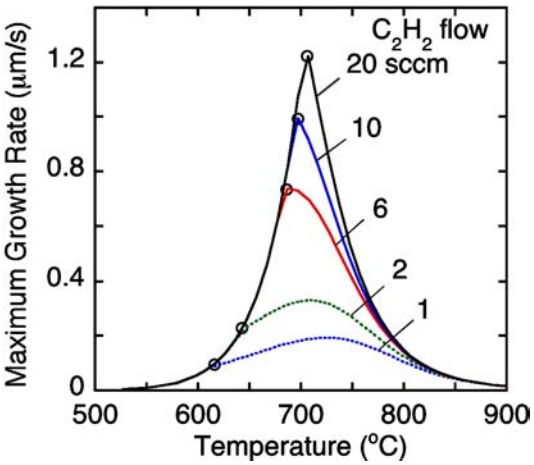

FIGURE 23 Calculated dependences of the maximum growth rate vs. temperature at different acetylene flow rates in the range 1–20 sccm

can be grown at lower temperatures if the partial pressure of the feedstock gas is relatively low (C_2H_2 flow $\leq$ 1–2 sccm). At higher flow ($\sim$ 10–20 sccm) the SWNTs start to grow at $\sim$ 700 °C, which coincides with our experimental finding based on Raman spectroscopy and high-resolution TEM. Basically, the increase of the partial acetylene pressure narrows the temperature window available for growth of the vertically aligned arrays of SWNTs.

To provide an alternative test of this model we considered two independent sets of the experimental data describing the feedstock partial pressure dependence of: (1) the growth rate (Fig. 15b) measured using the in situ reflectivity technique (Fig. 15a) and (2) the terminal length of VANTAs using ex situ SEM measurements. Basically, the model should predict an approximately constant maximum growth rate measured when the C_2H_2 flow was varied in the range from 2 to 19 sccm (Fig. 15b) and a relatively rapid increase in the terminal length of the VAA-CNTAs measured at these conditions (Fig. 15c).

Figure 23 clearly demonstrates that at relatively low temperatures ($\leq$ 650 °C) the maximum growth rate does not depend on the C_2H_2 flow in the considered flow range (2–20 sccm). The calculated dependence of the terminal length on C_2H_2 flow is shown in Fig. 15c. One can see that the calculations fit the experimental data quite well. The absolute values of the terminal length are larger than those measured experimentally, which is quite reasonable since the actual length of CNTs is higher compared to the array length because of the wiggling of the CNTs.

Although the kinetic model explains the whole set of the experimental data, it cannot identify any specific mechanism responsible for catalyst deactivation at higher temperatures. However, the model provides the basis for future experiments that could be used to complete this task.

8 Conclusions

Carbon nanotube growth kinetics have been directly measured in situ for the first time using time-resolved reflectivity (TRR) from vertically aligned arrays of carbon nanotubes (VANTAs) grown by chemical vapor deposition (CVD) from roughened metal catalyst films. The TRR technique takes advantage of Fabry–Perot fringes enabled by maintenance of a flat top surface of VANTAs as they grow. The mechanism of the coordinated growth is unclear, and will be addressed through time-resolved imaging measurements in future studies. Direct imaging of CNT growth combined with laser irradiation of VANTAs during growth indicated that the nanotubes grow predominantly from their bases [38].

In order to understand how catalyst nanoparticles form as the substrate is heated, in situ TRR was performed on Al-coated Si wafers with and without Mo/Fe catalyst films that were subjected to different thermal treatments. These data were correlated with AFM and SEM measurements of the resulting film morphologies. The results indicate that nanoparticles are formed due to oxidation of the Al underlayer. Oxidation occurs throughout the ramp-up of the oven temperature; however, the majority of surface roughening due to Al_2O_3 nanocrystal formation occurs below $\sim$ 410 °C (rms roughness $\sim$ 4 nm). As the temperature is increased above 450 °C, smoother surfaces (rms roughness $\sim$ 1.6 nm) are obtained, so it is concluded that heat released during the oxidation process may result in melting of the residual Al underlayer. Further experiments are required to fully understand the dynamics of the roughening process. However, it is clear that TRR provides a means for monitoring and control of oxidation and roughening to produce tailored nanoparticles for growth.

The Fabry–Perot fringes were found to provide constant increments in VANTA length as verified by arrested growth experiments. Conversely, each fringe corresponds to 300 $\pm$ 30 nm in VANTA length, so that TRR provides a reproducible method for controlling nanotube lengths in situ. Extinction of the laser beam may also be used to estimate the lengths of VANTAs. Calculations of the observed TRR signal were performed using the complex refractive indices for Si, VANTAs, and the surrounding gas. The effective complex refractive index, $1.075 + 0.045i$, was determined for VAA-CNTs by fitting the experimental TRR signal at 570 °C. The porosity of the VANTAs at 570 °C was estimated using the Looyenga formula as $\sim$ 0.92.

Growth rates of VANTAs were measured during CVD for temperatures between 535 and 900 °C, and the effect of different flow rates (concentrations) of C_2H_2 feedstock gas were separately studied. A narrow temperature window for growth of long arrays of vertically aligned carbon nanotubes was found around the temperature corresponding to the maximum in the absolute growth rate. The highest growth rates were achieved at 700 °C ($\sim$ 0.2 μm/s). For lower and higher temperatures the growth terminates after an initial growth spurt. At 700 °C, the growth continues to a few millimeters length at a growth rate of about 0.2 μm/s. Decreasing the partial pressure of the C_2H_2 feedstock gas increases the terminal length. Using the optimized growth conditions along with optimized catalyst films [39], we were able to grow up to 4.5-mm-long arrays of CNTs.

A kinetic model was constructed to fit both the growth rates and terminal lengths observed using TRR of the VANTAs for the different temperatures investigated in this study. Growth is modeled using rates for arrival of carbon on the metal catalyst surface, dissolution into a highly disordered, 'molten' surface catalyst layer that channels diffusion to the nanotube boundary, and precipitation into a nanotube. Termi-

FIGURE 24 Photographic image of a 3-mm-long carbon nanotube array grown on a 400-μm-thick Si wafer. A human image illustrates future goals and needs of VANTA synthesis for practical applications. At present, person not to scale, however the combination suggests the possibilities if growth rates and terminal lengths for VANTAs continue to improve at the present pace

nation of growth was modeled by assuming catalyst poisoning either by over-coating or deactivating active sites on the catalyst surface. In the framework of this model the number of CNT walls is described by the thickness of the disordered layer on the surface of the catalyst nanoparticle.

The terminal length of the VAA-CNT determined experimentally exponentially depends on $1/T$ for $T \leq 700\,^{\circ}\mathrm{C}$. The model predicts this dependence and provides a simple way to determine the activation energy difference, $\Delta E = E_{\mathrm{sb}} - E_{\mathrm{cl}}$. An analytical solution for the length of the nanotube arrays vs. time was derived in (11), which indicates that growth in this regime is determined principally by the ratio of dissolution to poisoning ($k_{\mathrm{sb}}/k_{\mathrm{cl}}$) on the catalyst surface with the absolute magnitude of the growth rate depending on the arrival rate of carbon via the flux F_{c1}. The model shows that the temperature behavior of the terminal length is defined by two competing processes: (1) activation of the catalyst nanoparticle defined by the activation barrier, E_{sb}, and (2) deactivation of its catalytic activity due to poisoning of the catalyst nanoparticle defined by the activation barrier, E_{p} or E_{r}, depending on the specific deactivation mechanism. The high-temperature drop-off in terminal length can be used to estimate activation energy for the poisoning process (see Fig. 19). However, only from time-resolved data (see Fig. 13) can details of the kinetics be assessed. Two poisoning processes were considered: (1) a quadratic dependence on feedstock pressure because of binary collisions that form gas-phase pyrolysis products and (2) catalyst deactivation due to a first-order process such as changes in the oxidation state of the catalyst nanoparticle due to hydrogen reduction or direct oxygen desorption.

The model indicates that the first assumption cannot explain the observed temperature and pressure dependences of the growth rate, permitting elimination of gas-phase pyrolysis products as a major source of catalyst deactivation at higher temperatures. The second assumption is consistent with the measured temperature and pressure dependences of the VANTA growth rates as well as their terminal lengths.

The ability to predict the number of CNT walls at different temperatures and feedstock pressures supports our hypothesis of the highly disordered 'molten skin' on the surface of a catalyst nanoparticle. Using this assumption, the onset for growth of SWNTs is predicted and temperatures and feedstock pressures for growth of SWNT arrays (see Fig. 23) are specified.

In summary, this paper describes how time-resolved reflectivity is applied for in situ monitoring and control of catalyst film pretreatment and for measurements of growth kinetics of vertically aligned arrays of CNTs. These data were used to develop a simplified rate-equation model which reasonably fits the experimental growth kinetics, and specifies the conditions for growth of VANTAs with a defined number of walls, e.g. DWNTs or SWNTs. This study provides a clear way to grow long and dense arrays of carbon nanotubes over large surface areas (Fig. 24) for a variety of different applications including, for example, carbon nanotube polymer composites with enhanced and directional thermal conductivities.

ACKNOWLEDGEMENTS The authors gratefully acknowledge the technical assistance of Pam Fleming, discussions with R.F. Wood, J.C. Wells, S. Pannala, and I.A. Merkulov, the assistance with TEM analysis of J.Y. Howe, and funding support from the US Department of Energy under Contract No. DE-AC05-00OR22725 with the Oak Ridge National Laboratory, managed by UT-Battelle, LLC and the Laboratory-Directed Research and Development Program at ORNL and DARPA-DSO.

REFERENCES

1 H. Dai: Acc. Chem. Res. **35**, 1035 (2002)
2 R. Andrews, D. Jacques, D. Qian, T. Rantell: Acc. Chem. Res. **35**, 1008 (2002)
3 R.T.K. Baker: Carbon **27**, 315 (1989)
4 S. Helveg, C. Lopez-Cartes, J. Sehested, P.L. Hansen, B.S. Clausen, J.R. Rostrrup-Nielsen, F. Abild-Petersen, J.K. Norskov: Nature **427**, 426 (2004)
5 J.-M. Bonard, M. Croci, F. Conus, T. Stöckli, A. Chatelain: Appl. Phys. Lett. **81**, 2836 (2002)
6 D.B. Geohegan, A.A. Puretzky, I.N. Ivanov, S. Jesse, G. Eres, J.Y. Howe: Appl. Phys. Lett. **83**, 1851 (2003)
7 D.H. Kim, H.S. Jang, C.D. Kim, D.S. Cho, H.S. Yang, H.O. Kang, B.K. Min, H.R. Lee: Nanoletters **3**, 863 (2003)
8 X. Zhang, A. Cao, B. Wei, Y. Li, J. Wei, C. Xu, D. Wu: Chem. Phys. Lett. **362**, 285 (2002)
9 Y.T. Lee, J. Park, Y.S. Choi, H. Ryu, H.J. Lee: J. Phys. Chem. B **106**, 7614 (2002)
10 Z.W. Pan, S.S. Xie, B.H. Chang, C.Y. Wang, L. Lu, W. Wu, W.Y. Zhou, W.Z. Li, L.X. Qian: Nature **394**, 631 (1998)
11 L. Delzeit, C.V. Nguyen, B. Chen, R. Stevens, A. Cassell, J. Han, M. Meyyappan: J. Phys. Chem. B **106**, 5629 (2002)
12 K. Jiang, Q. Li, S. Fan: Nature **419**, 801 (2002)
13 G. Eres, A.A. Puretzky, D.B. Geohegan, H. Cui: Appl. Phys. Lett. **84**, 1759 (2004)
14 L. Delzeit, B. Chen, A. Cassell, R. Stevens, C.V. Nguyen, M. Meyyappan: Chem. Phys. Lett. **348**, 368 (2001)
15 H. Cui, G. Eres, J.Y. Howe, A. Puretzky, M. Varela, D.B. Geohegan, D.H. Lowndes: Chem. Phys. Lett. **374**, 222 (2003)
16 K. Ujihara: J. Appl. Phys. **43**, 2376 (1972)
17 L.P.H. Jeurgens, W.G. Sloof, F.D. Tichelaar, E.J. Mittemeijer: J. Appl. Phys. **92**, 1649 (2002)
18 'The Standard Enthalpy of Formation of Al_2O_3 (Corundum) is -1675.7 ± 1.3 kJ/mol'. In: *Handbook of Chemistry and Physics*, 77th edn., ed. by D.R. Lide (CRC, Boca Raton, New York, London, Tokyo 1996–1997) p. 5-1

19 *Constitution of Binary Alloys*, 2nd edn. (Metall. Metall. Eng. Ser.), ed. by M. Hansen (McGraw-Hill, New York, Toronto, London 1958) pp. 132–134
20 Q. Jiang, H.Y. Tong, D.T. Hsu, K. Okuyama, F.G. Shi: Thin Solid Films **312**, 357 (1998)
21 M. Zhang, M.Yu. Efremov, F. Schiettekatte, E.A. Olson, A.T. Kwan, S.L. Lai, T. Wisleder, J.E. Greene, L.H. Allen: Phys. Rev. B **62**, 10 548 (2000)
22 T. de los Arcos, Z.M. Wu, P. Oelhafen: Chem. Phys. Lett. **380**, 419 (2003)
23 W. Theiss: Surf. Sci. Rep. **29**, 91 (1997)
24 G.E. Jellison, Jr., F.A. Modine: J. Appl. Phys. **76**, 3758 (1994)
25 E.A. Rohlfing: J. Chem. Phys. **118**, 7622 (2003)
26 R.T.K. Baker, P.S. Harris: in *Chemistry and Physics of Carbon, Vol. 14*, ed. by P.L. Walker, Jr., P.A. Thrower (Marcel Dekker, New York, Basel 1978) p. 102
27 R.T.K. Baker, M.A. Barber, P.S. Barber, P.S. Harris, F.S. Feates, R.J. Waite: J. Catal. **26**, 51 (1972)
28 H. Kanzow, A. Schmalz, A. Ding: Chem. Phys. Lett. **295**, 525 (1998)
29 O.A. Louchev, T. Laude, Y. Sato, H. Kanda: J. Chem. Phys. **118**, 7622 (2003)
30 O.A. Louchev, T. Laude, Y. Sato, H. Kanda: Phys. Rev. E **66**, 011 601 (2002)
31 W.H. Hung, S.L. Bernasek: Surf. Sci. **339**, 272 (1995)
32 G.D. Lee, S. Han, J. Yu, J. Ihm: Phys. Rev. B **66**, 081 403-1 (2002)
33 O.A. Louchev, Y. Sato, H. Kanda: Appl. Phys. Lett. **80**, 2752 (2002)
34 F. Ding, K. Bolton, A. Rosen: J. Vac. Sci. Technol. A **22**, 1471 (2004)
35 K. Hata, D.N. Futuba, K. Mizuno, T. Namai, M. Yumura, S. Iijima: Science **306**, 1362 (2004)
36 T. Tanzawa, W.C. Gardiner, Jr.: J. Phys. Chem. **84**, 236 (1980)
37 M. Frenklach, S. Taki, M.B. Durgaprasad, R.A. Matula: Combust. Flame **54**, 81 (1983)
38 D.B. Geohegan, A.A. Puretzky, G. Eres, I.N. Ivanov: to be published
39 H.M. Christen, A.A. Puretzky, H. Cui, K. Belay, P.H. Fleming, D.B. Geohegan, D.H. Lowndes: Nanoletters **4**, 1939 (2004)